Supplementary Information:

A Robust Gradient Solid Electrolyte Interphase Enables Fast Zn Dissolution and Deposition Dynamics

Caiyun Chang[#ab], Sanlue Hu[#ab], Titi Li[a], Fanbin Zeng[a], Dun Wang[ac], Songde Guo[ac], Minwei Xu[ab], Guojin Liang[ab], Yongbing Tang[ab], Hongfei Li[*c], Cuiping Han[*ab] and Hui-Ming Cheng[*abd]

[a] *Faculty of Materials Science and Energy Engineering/Institute of Technology for Carbon Neutrality, Shenzhen Institute of Advanced Technology, Chinese Academy of Sciences, Shenzhen 518055, China. E-mail: cp.han@siat.ac.cn; hm.cheng@siat.ac.cn.*

[b] *Shenzhen Key Laboratory of Energy Materials for Carbon Neutrality, Shenzhen Institute of Advanced Technology, Chinese Academy of Sciences, Shenzhen 518055, China.*

[c] *School of System Design and Intelligent Manufacturing, Southern University of Science and Technology, Shenzhen 518055, China. E-mail: lihf@sustech.edu.cn.*

[d] *Shenyang National Laboratory for Materials Science, Institute of Metal Research, Chinese Academy of Sciences, Shenyang 110016, China.*

# These authors contributed equally to this work.

Experimental Section

Reagents and Materials

Zinc trifluoromethanesulfonate ($Zn(OTf)_2$, 98%) was purchased from the Shanghai Macklin Biochemical Co. Dimethylformamide (DMF, 99.5%), fluorinated 2,2,2-trifluoro-*N, N*-dimethylacetamide (DMTFA, 95.0%), sodium hydroxide (NaOH, 96%), and vanadium pentoxide (V_2O_5, 96%) were purchased from the Aladdin Biochemical Technology Co. All chemicals were directly used without further purification. The deionized water was purified on a MilliQ device from Millipore (18 MΩ cm^{-2} at 25℃). Glass fiber separator (Whatman, 47 mm) was provided by Shanghai Huanao Technology Ltd.

Preparation of Electrolytes and Electrode

Electrolyte preparation. The modified electrolyte was prepared by dissolving 1.2 M $Zn(OTf)_2$ into H_2O: DMF: DMTFA with a molar ratio of 1:1:1 (labeled ternary electrolyte). The $Zn(OTf)_2$−DMF−H_2O electrolyte (labeled binary electrolyte) was prepared by dissolving 1.2 M $Zn(OTf)_2$ into H_2O: DMF with a molar ratio of 1:1. The $Zn(OTf)_2$−H_2O electrolyte (labeled baseline electrolyte) was prepared by dissolving 1.2 M $Zn(OTf)_2$ into deionized water. The electrolytes were stirred for 48 hours at room temperature before use.

NaV_3O_8 (NVO) electrode fabrications. 0.400 g NaOH and 1.819 g V_2O_5 were mixed and dissolved in 40 ml deionized water (H_2O) under stirring for 0.5 h. Then the mixture solution was transferred into a polytetrafluoroethylene reactor and maintained at 200℃ for 48 h. The obtained precursor was washed with (H_2O) and ethanol, then dried at 80℃ for 12 h in a vacuum oven. Finally, NVO nanorods were fabricated and calcined at 300℃ for 2 h in a muffle furnace (Fig. S33). To prepare the NVO cathode electrode, the obtained NVO was mixed with ketjenblack and PVDF in NMP with a mass ratio of 7:2:1, and casing the slurry on carbon cloth or Ti mesh. The electrodes were dried at 60℃ for 24 h. The carbon cloth-based electrode was cut to get a 12 mm diameter disc, and the NVO loading was ~3 mg cm^{-2}. The Ti mesh-based electrode of 4 cm × 5 cm was cut for assembling a pouch cell and the NVO loading was ~11.5 mg cm^{-2}.

Characterizations

The chemical structures of the solvents and electrolytes were characterized by NMR (400 MHz, Bruker Ascend400), FTIR spectra, and Raman spectroscopy (532 nm, Horiba LabRAM HR800). For the ^{1}H NMR test, D_2O was used as the internal standard. The ionic conductivities of electrolytes were measured by an ionic conductivity meter (Leici, DDSJ-319L). The surface morphology of cycled Zn anode was viewed using SEM (Hitachi SU4800), and TEM (Tecnai F30 TEM) with a Gatan Continuum EELS spectrometer. The SEI layer components were investigated by TOF-SIMS analysis using a TRIFT V nanoToF II equipped with a 30 kV Au-LMIG. In-situ observations of Zn deposition behaviors were detected on optical microscopy (6XB-PC, Optical Instrument Factory). The chemical bonding environments were probed by XPS via a PHI 5000 Versa Probe II spectrometer. XRD analysis was carried out by a Rigaku Miniflex600 diffractometer equipped with Cu Kα radiation. Young's modulus and hardness of the formed SEI on the Zn surface were measured by a nanoindentation test (Nano indenter G200, USA) with a laser scanning confocal microscope and AFM (Bruker, Dimension icon) with the quantitative nanomechanics mode. SECM measurements were performed using a three-electrode system on BioLogic M470.

Density functional theory (DFT) calculations

The DFT calculations were carried out in the Gaussian 16 package[1] with Becke's three-parameter hybrid method using the Lee–Yang–Parr (B3LYP)[2] correlation functional at 6-31G(d, p) level[3]. Besides, the DFT-D3 (Becke-Johnson) method was taken into account for the effect of the van der Waals interactions of these calculations[4, 5]. After optimization and single-point calculations, the visualizations of the LUMO and HOMO results were using the Multiwfn[6] and VMD[7] software.

Molecular dynamics (MD) simulations

The MD simulations for the electrolyte systems were performed using the GROMACS 2022.4 simulation package.[8] An all-atom optimized potential for liquid simulations (OPLS-AA) force field was employed.[9] The OPLS-AA force field with a scaling factor of 0.8 was utilized for the anion OTf^-, based on previous work.[10] The

OPLS-AA force field parameters of the molecules H_2O, DMF, and DMTFA were established by the Ligpargen web server.[11-13] The molecules $Zn(OTf)_2$, H_2O, DMF, and DMTFA were optimized by the B3LYP/6-31g(d, p) level of the Gaussian 16 package, with the inclusion of the DFT-D3 (Becke-Johnson) method to account for the effect of the van der Waals interactions before simulations. The atomic charge distributions of these molecules were obtained using the restrained electrostatic potential 2 (RESP2) charge calculation through Gaussian and Multiwfn software to obtain more accurate charges. The initial periodic models were built by using the PACKMOL package and the simulation boxes were set to 3 nm×3 nm×3 nm.[14] The MD simulation procedure consisted of five steps: two-step energy minimization, two-step pre-equilibration, and a production simulation step. The energy minimization process involved a 20000-step steep descent method followed by a 20000-step conjugate gradient method. Subsequently, the system was pre-equilibrated in the constant-temperature, constant-volume (NVT) ensemble with V-rescale coupling at 298.15 K for 100ps, followed by the constant-temperature, constant-pressure ensemble (NPT) with V-rescale coupling/Berendsen barostat at ambient pressure and temperature (1.01325 bar, 298.15K) for 2 ns. For production simulation, an NPT ensemble with V-rescale coupling and Berendsen barostat at ambient pressure and temperature (1.01325 bar, 298.15K) for 20 ns. A time step of 2 fs and the Particle−Mesh−Ewald (PME) method was employed for all simulations.[15] The results of the final production simulation used radial distribution function (RDF) and coordination structure counting methods, and the visualizations of the MD simulations were carried out using the VESTA and VMD software.[16]

Electrochemical measurements

Zn foil (100 μm, 99.9%) was polished with abrasive paper and cleaned with ethanol to remove the passivation layer. Zn foil was cut into a disc (ϕ = 12 mm) to be applied as an anode. Cu foil (10 μm, 99.99%) and Ti foil (10 μm, 99.99%) were cut into a disc (ϕ = 16 mm) to be applied as a cathode for Zn||Cu and Zn||Ti cells. All the testing CR2032 coin cells were assembled in an open-air environment by using a glass fiber

separator with 120 μl electrolytes and tested on a battery test system (Neware). The Zn||Cu and Zn||Ti cells were assembled to measure CE, and the Zn||Zn cells were used to assess the reversibility of Zn plating/ stripping. The Zn||NVO full pouch cell (4 cm × 5 cm) was configured to evaluate the energy and power density using Zn foil (50 μm thickness) and thick NVO electrode (loading of ~11.5 mg cm^{-2}) by adding 4 ml electrolyte (Fig. 7e, insert). The GCD cycles were performed in a potential range of 0.2~1.6 V (Zn^{2+}/Zn). EIS measurements were conducted on a VSP-3e Potentiostat electrochemical workstation (BioLogic) with frequencies ranging from 100 kHz to 50 mHz. CV tests were also investigated on electrochemical workstations with various scan rates. The nucleation overpotential of Zn was operated on the electrochemical workstation with a three-electrode system (Ag/AgCl as reference electrode, Zn foil as working and counter electrode). To evaluate the oxidation-reduction potential with LSV, a three-electrode system (Ag/AgCl as reference electrode, Ti foil as working electrode, and Pt as counter electrode) with the sweeping rate at 1 mV s^{-1} at the voltage range of -1.0~2.8 V. The transference number is calculated by a current-time curve under potentiostatic polarization at 5 mV for 5000 seconds. The Tafel curves were conducted on a three-electrode system with Ag/AgCl as a reference, Pt foil as the counter electrode, and Zn foil as the working electrode.

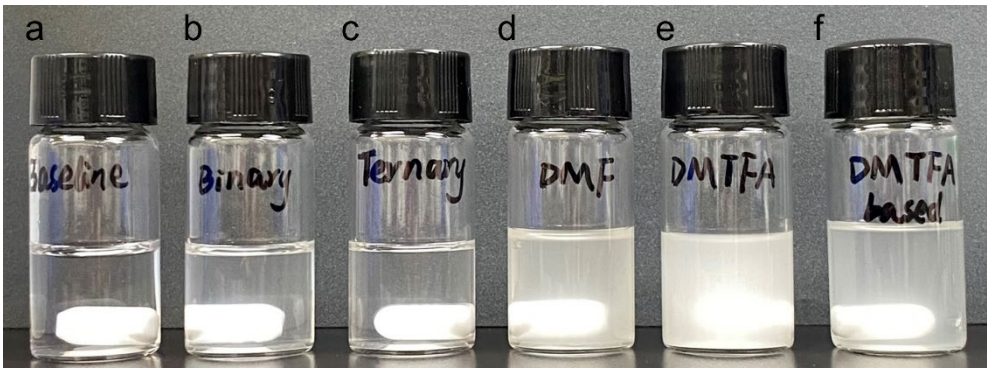

Fig. S1 The solubility of 1.2 M $Zn(OTf)_2$ in DMTFA, DMF, and H_2O solution. (a) 1.2 M $Zn(OTf)_2$ was completely dissolved into H_2O, which was labeled as the baseline electrolyte. (b) 1.2 M $Zn(OTf)_2$ was completely dissolved into H_2O:DMF with molar ratio of 1:1, which was labeled as the binary electrolyte. (c) 1.2 M $Zn(OTf)_2$ was completely dissolved into H_2O: DMF: DMTFA with the molar ratio of 1:1:1, which was labeled as the ternary electrolyte. (d, e) 1.2 M $Zn(OTf)_2$ was completely dissolved into DMTFA or DMF, respectively. As a sharp contrast, $Zn(OTf)_2$ was only slightly dissolved in DMTFA. (f) 1.2 M $Zn(OTf)_2$ was dissolved into the mixed solution of H_2O: DMTFA with a molar ratio of 1:1, which was labeled as the DMTFA-based electrolyte.

The design principles based on the aqueous electrolyte for AZIBs:

First, the functional solvent has the characteristics of low cost, low flammability, low lowest unoccupied molecular orbital (LUMO) energy levels, and high voltage potential; Second, the electrolyte components can be mixed into a homogeneous solution or can be mixed after treatment but cannot react with each other, that is, the functional components can exist stably in water; Second, for the hydrogen evolution reaction (HER) in aqueous zinc-ion batteries, the functional solvent of electrolyte should contain the lone pair electrons to provide hydrogen bond (H-bond) acceptance sites to form the intermolecular H-bonds, thus reducing the activity of the free water; Finally, the optimal chemical solvent should be capable of constructing a dense and complete SEI layer on the electrode by decomposing preferentially to form a kinetic barrier of HER.

According to the above requirements for functional solvents, the solvents that meet the conditions are the strong electron-withdrawing amide O=C-N group from amides and sulfonyl O=S=O group from sulfones.

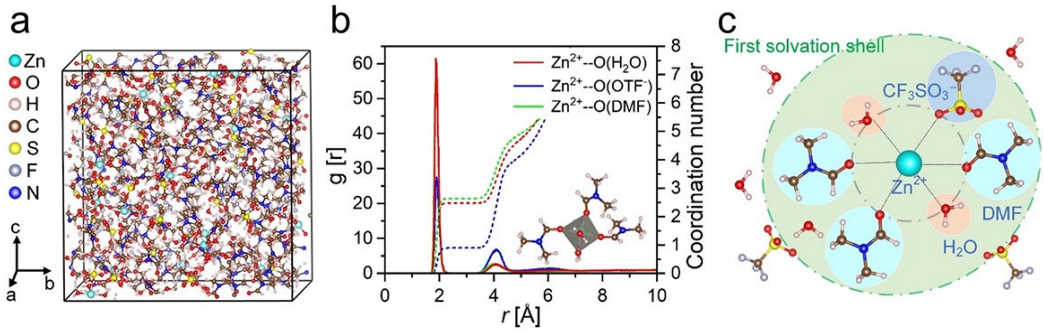

Fig. S2 Zn^{2+}- solvation structure of the binary electrolyte. (a) 3D snapshots of the MD simulation of the binary electrolyte. (b) RDFs and corresponding coordination numbers for Zn^{2+}-O (H_2O), Zn^{2+}-O (OTf^-), and Zn^{2+}-O (DMF) of the binary electrolyte. Insets present the Zn^{2+} ions coordination structure in the binary electrolyte. (c) Schematic illustrations of Zn^{2+}-solvated structure for the binary electrolyte.

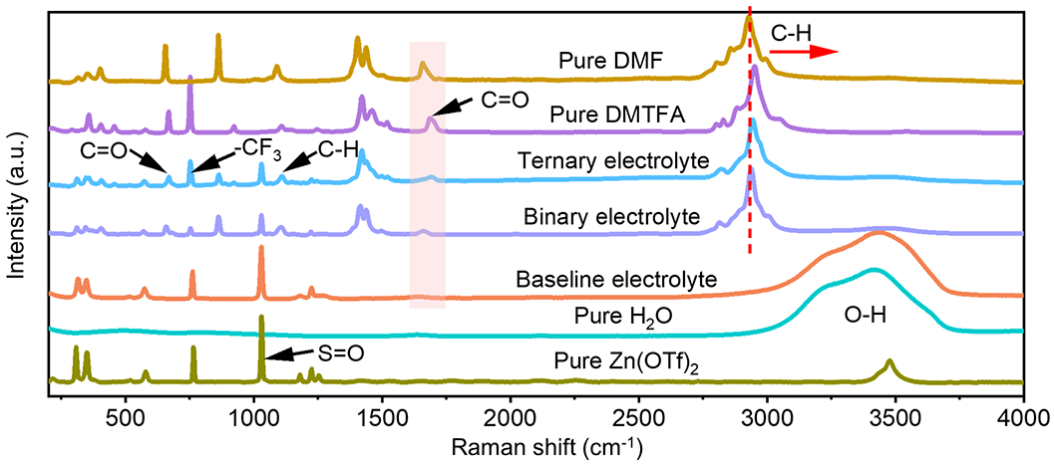

Fig. S3 Raman spectra of pure $Zn(OTf)_2$ salt, pure H_2O solvent, pure DMF solvent, pure DMTFA solvent, the baseline electrolyte, binary electrolyte, and ternary electrolyte.

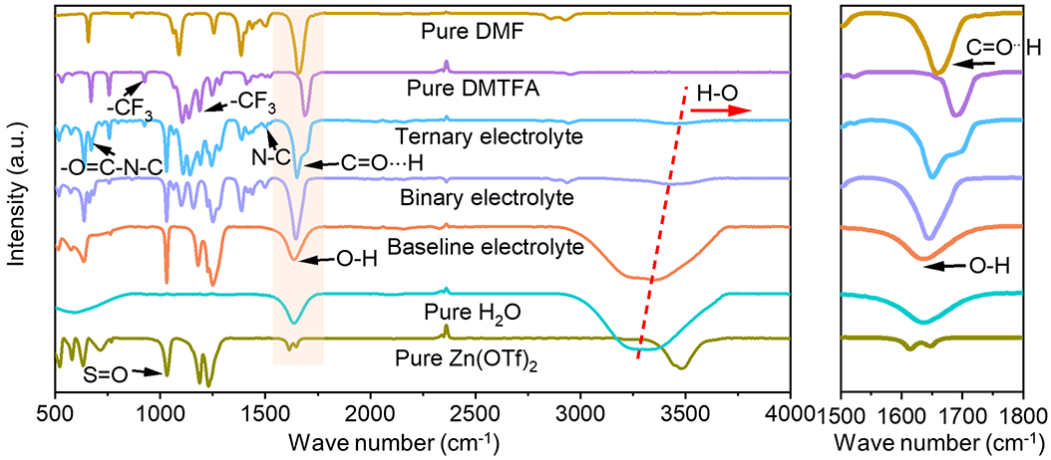

Fig. S4 FTIR spectra of pure $Zn(OTf)_2$ salt, pure H_2O solvent, pure DMF solvent, pure DMTFA solvent, the baseline electrolyte, binary electrolyte, and ternary electrolyte. The right figure is enlarged portions of 1500~1800 cm^{-1}.

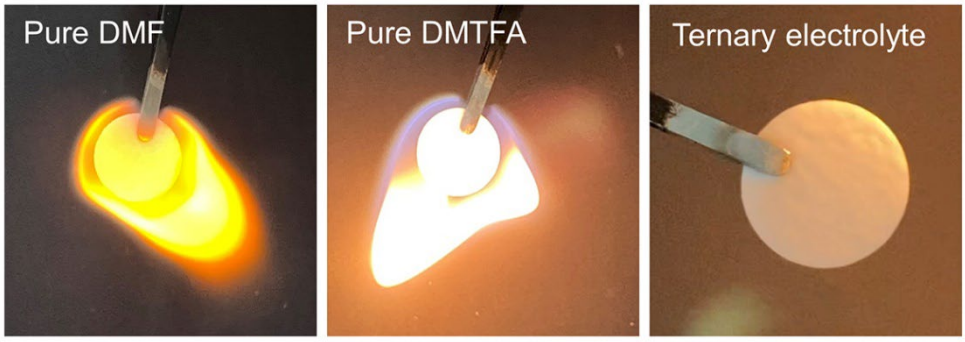

Fig. S5 Digital images of flammability tests of pure DMF, pure DMTFA, and the ternary electrolyte.

During the combustion test, the glass fibers absorbing pure DMF and pure DMTFA solvents can be ignited immediately, while the glass fibers absorbing various electrolytes exhibit non-flammability (Movie S1).

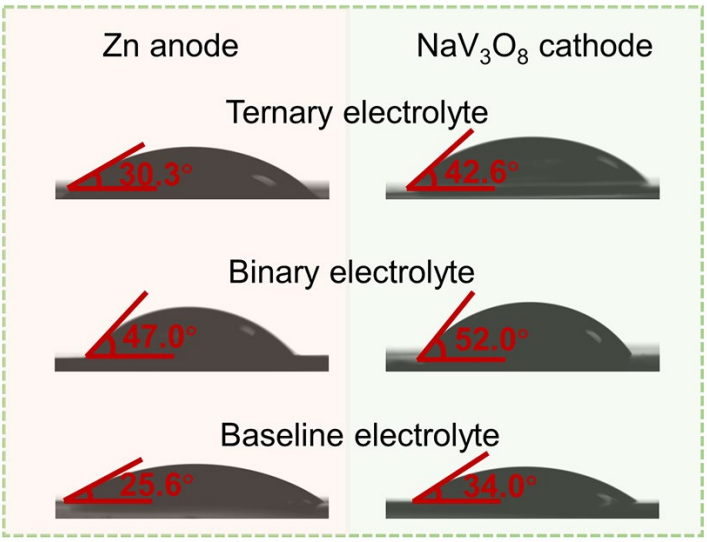

Fig. S6 Photos of the contact angles of the baseline electrolyte, binary electrolyte, and ternary electrolyte on the Zn anode and NaV_3O_8 cathode surfaces.

Before tests, the Zn anode surfaces were polished with abrasive paper and cleaned with ethanol to remove the passivation layer. NaV_3O_8 cathode electrode was prepared by mixing NaV_3O_8 powder, ketjenblack, and PVDF in NMP with a mass ratio of 7:2:1, then the slurry was coated on Ti foil. The droplet size is 4 μl.

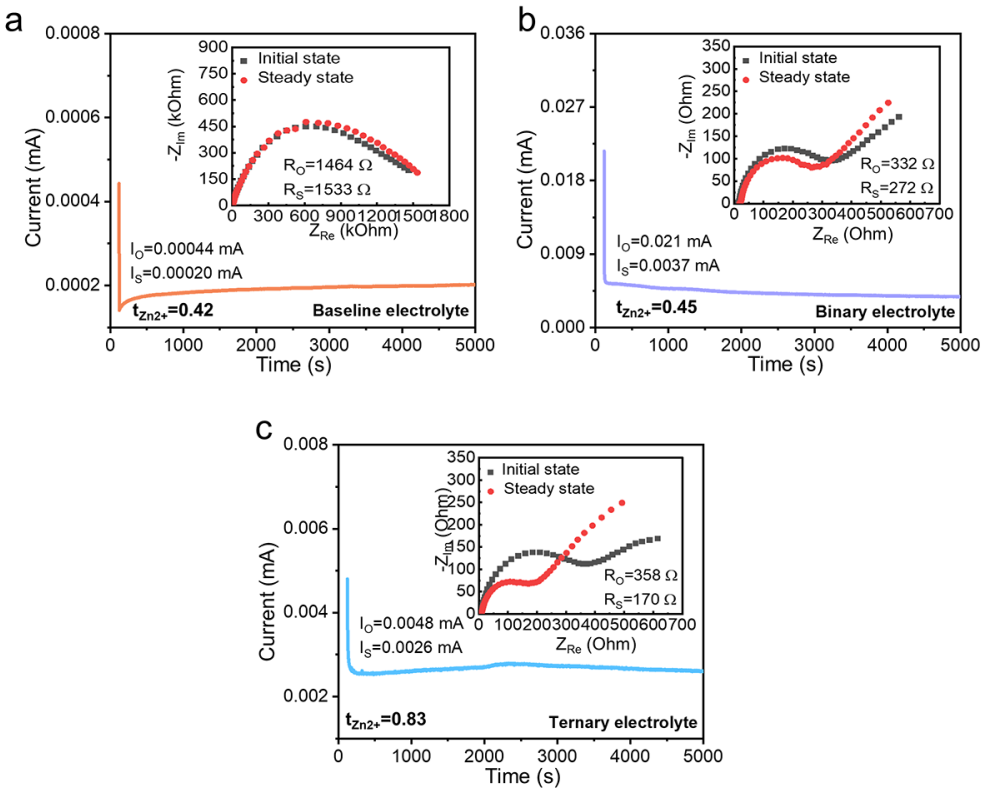

Fig. S7 The Zn^{2+} transference number measurement of (a) the baseline electrolyte, (b) binary electrolyte, and (c) ternary electrolyte in Zn||Zn symmetric cells.

The chronoamperometry and EIS test was carried out. The equation was used to calculate the Zn^{2+} transference number (t_{Zn}^{2+}):

$$t_{Zn2+} = \frac{I_s(\Delta V - I_0 R_0)}{I_0(\Delta V - I_s R_s)}$$

where ΔV is the applied voltage across the cell of 5 mV, and the I_0, I_S, R_0, and R_S are the initial current, steady-state current, initial impedance, and steady-state impedance of the measured cells, respectively.

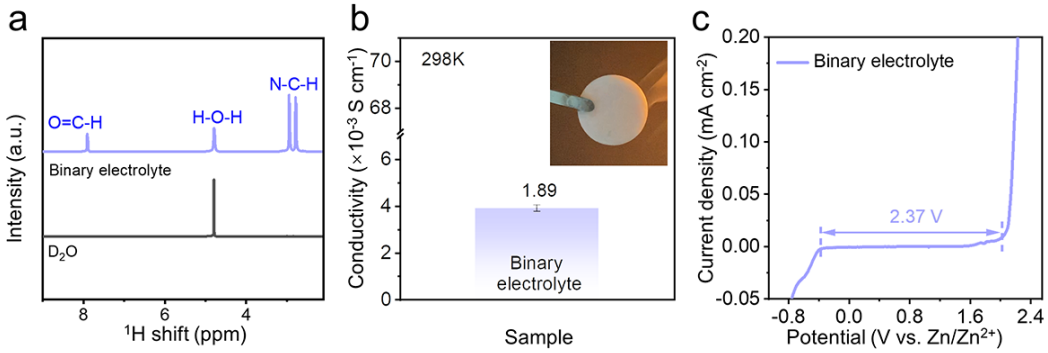

Fig. S8 Physicochemical and electrochemical characterizations of the binary electrolyte. (a) ^{1}H NMR spectra of pure D_2O and the binary electrolyte. (b) The ion conductivity and (c) LSV curve of the binary electrolyte at 25℃.

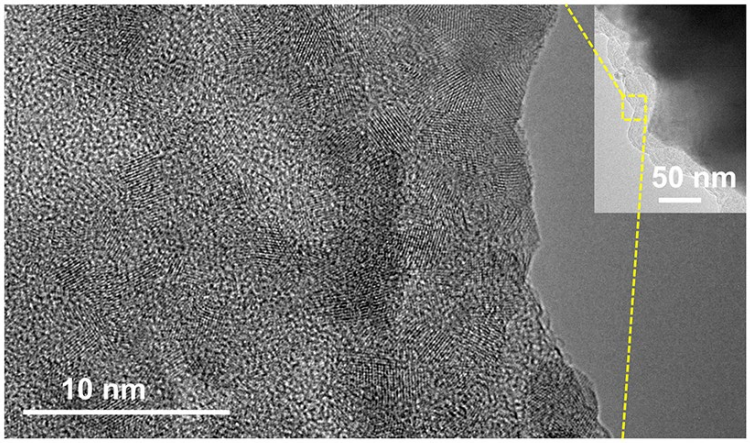

Fig. S9 The high-resolution TEM image of the SEI obtained from the yellow rectangle of the inset. The inset shows the low-magnification TEM image of the deposited Zn on the Cu mesh at 1 mA cm^{-2} for 1 h in the ternary electrolyte. The SEI layer was homogeneous and integrity.

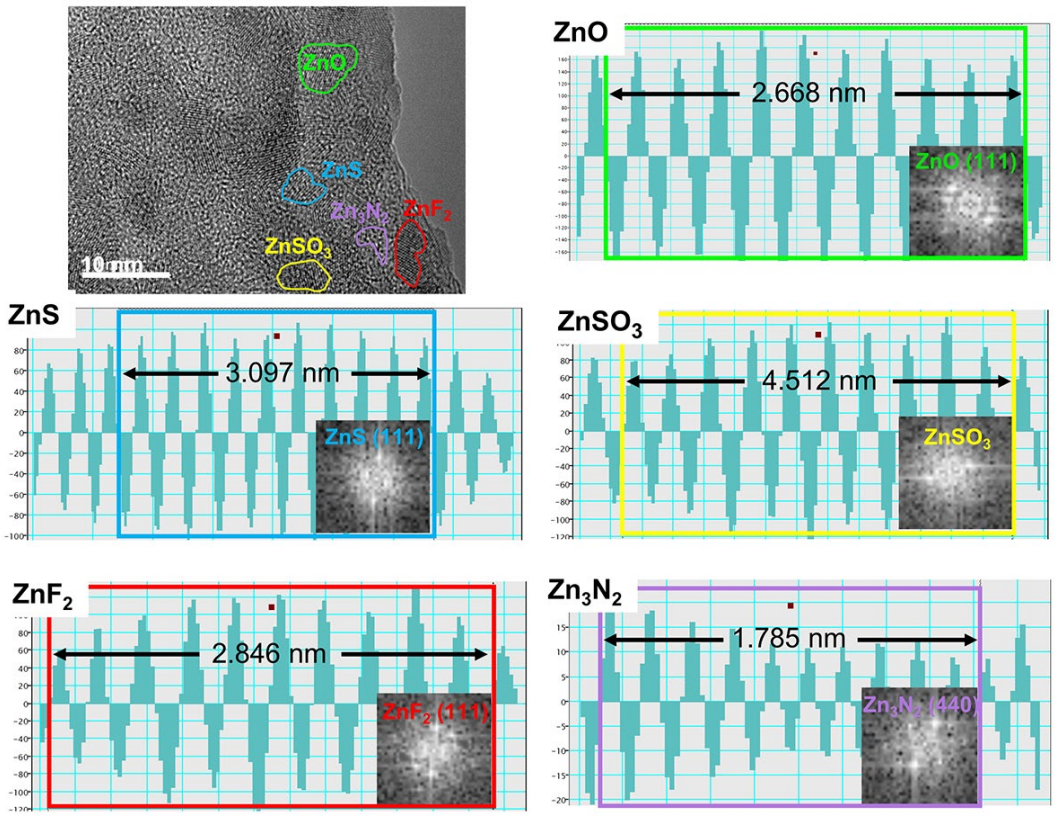

Fig. S10 The high-resolution TEM image of the SEI and the periodicity of the representative Moire fringes corresponding to the crystals. Inserts show the corresponding fast Fourier-transform (FFT) patterns.

The SEI was obtained from the deposited Zn on the Cu mesh at 1 mA cm^{-2} for 1 h by using the ternary electrolyte. Significantly, the existence of crystalline ZnO, ZnS, $ZnSO_3$, ZnF_2, and Zn_3N_2 are exhibited, which have been marked with different colors at the corresponding positions. These crystalline structures are classified according to the corresponding lattices and the FFT patterns, such as ZnO (111), ZnS (111), etc.

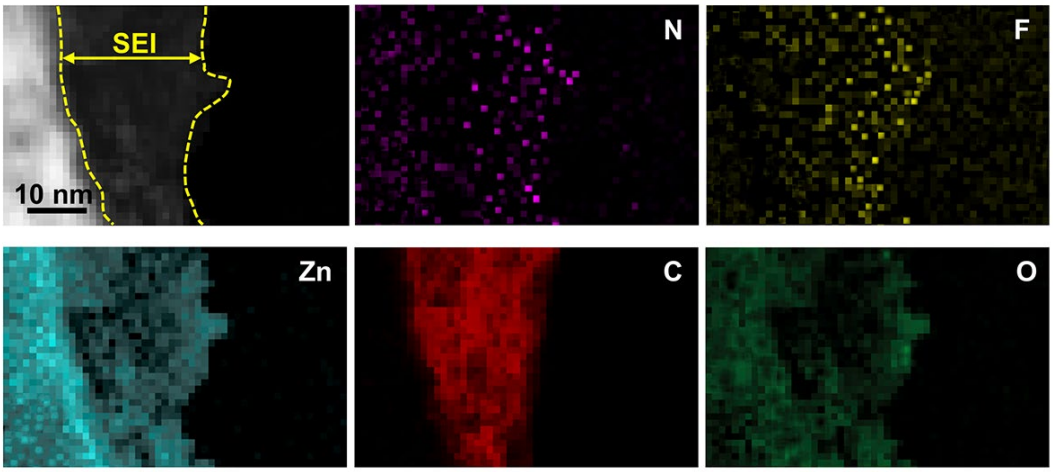

Fig. S11 The high-resolution TEM image of the deposited Zn and the corresponding EELS elements maps of N, F, Zn, C, and O elements.

The N and F elements mainly exist inside the SEI layer and the Zn, O, and C continuously distribute throughout the SEI, especially the carbon element. This result demonstrates that the components of the SEI on the Zn surface in the ternary electrolyte show an outside organic and inside gradient-inorganic distribution, indicating the complete decomposition of OTf^-, DMF, and DMTFA. On the one hand, the inorganic zinc salts-rich species with high interphase energy and low adhesion are mainly distributed on the interlayer of the SEI, which contributes to promoting the uniform spherical deposition of zinc below it. On the other hand, organic-rich components of the outside layer show excellent structural integrity to block the direct contact of water and ZMA for inhibiting the severe corrosion of electrolytes and accommodating the volume change during the Zn plating/striping.

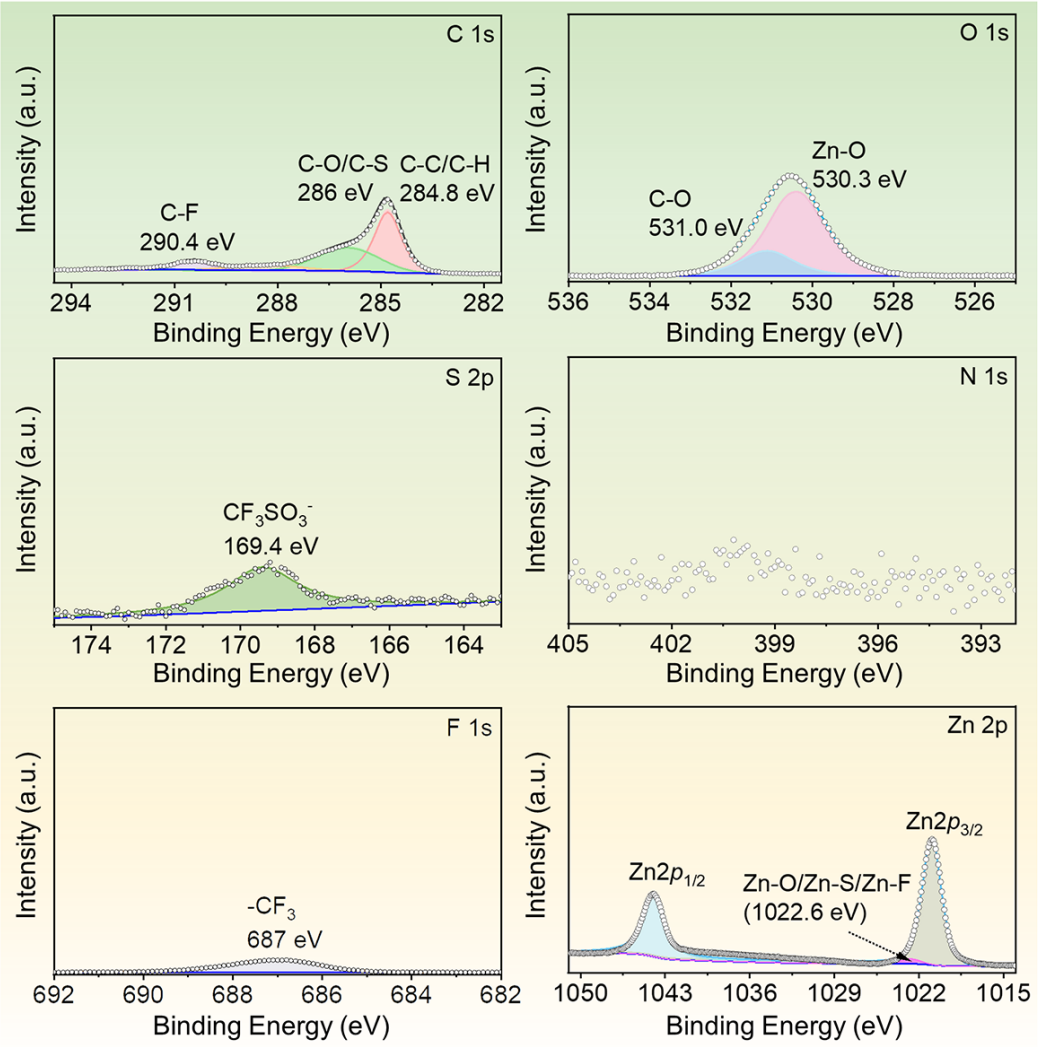

Fig. S12 C 1s, O 1s, S 2p, N 1s, F 1s, and Zn 2p XPS spectra of the plated Zn topmost surface after 10 cycles in the baseline electrolyte.

Generally, the C-element from the organic components of the SEI layer is characterized. However, the peaks related to the C element are relatively weak for the formed SEI in the baseline electrolyte, indicating the lack of a stable organic SEI layer. Moreover, the $CF_3SO_3^-$ stemming from $Zn(OTf)_2$ is hardly decomposed, that is, there is only a tiny amount of $-CF_3$ in F 1s, suggesting the stability of the OTf^- in the baseline electrolyte during Zn plating/stripping process. Anyway, the Zn anode surface lacks the stable SEI layer in the baseline electrolyte.

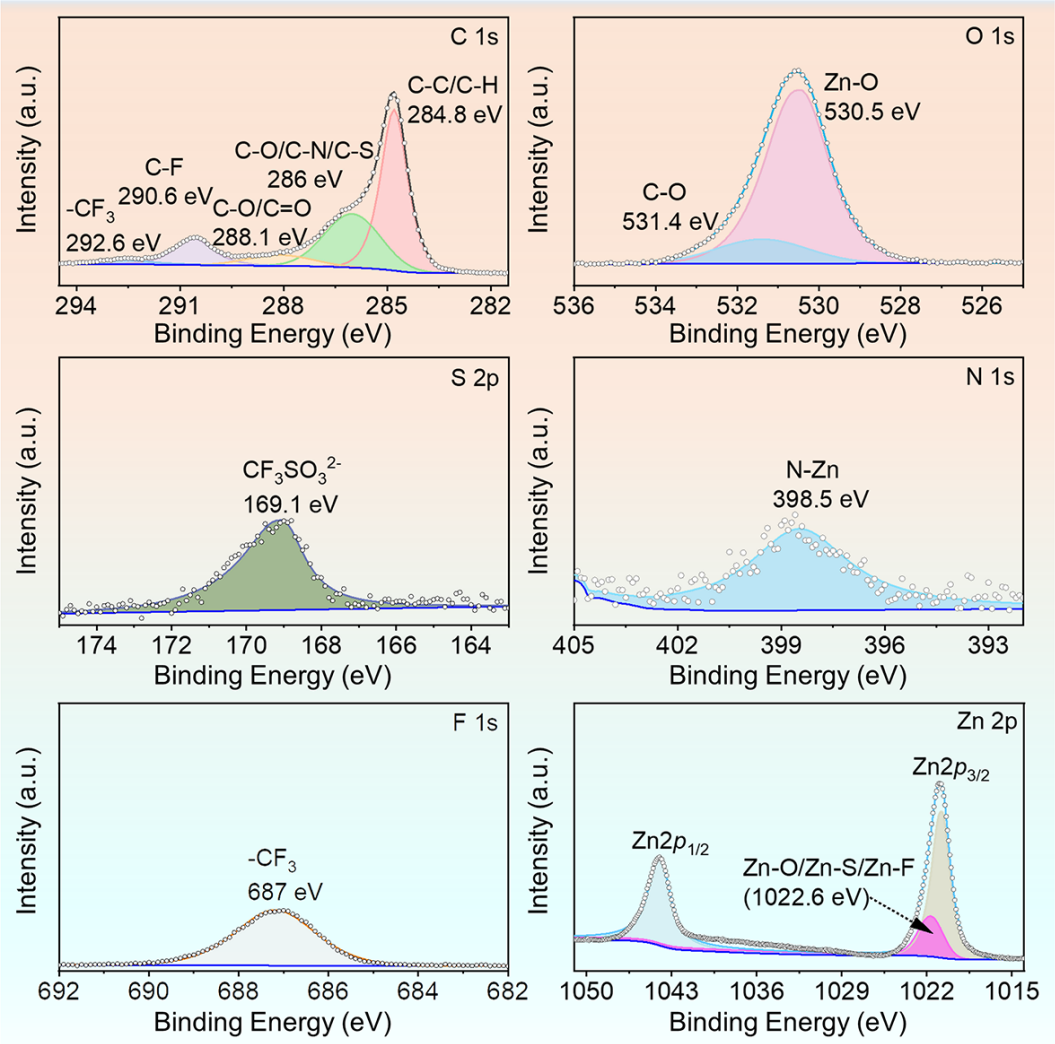

Fig. S13 C 1s, O 1s, S 2p, N 1s, F 1s, and Zn 2p XPS spectra of the plated Zn topmost surface after 10 cycles in the binary electrolyte.

The Zn anode surface presents the SEI layer, which consists of organic and inorganic components stemming from the decomposition of DMF and OTf^-. This result illustrates that the addition of low-LUMO DMF contributes to modulating the Zn^{2+} inner solvation-sheath structure to reduce the coordination number of Zn^{2+} and H_2O.

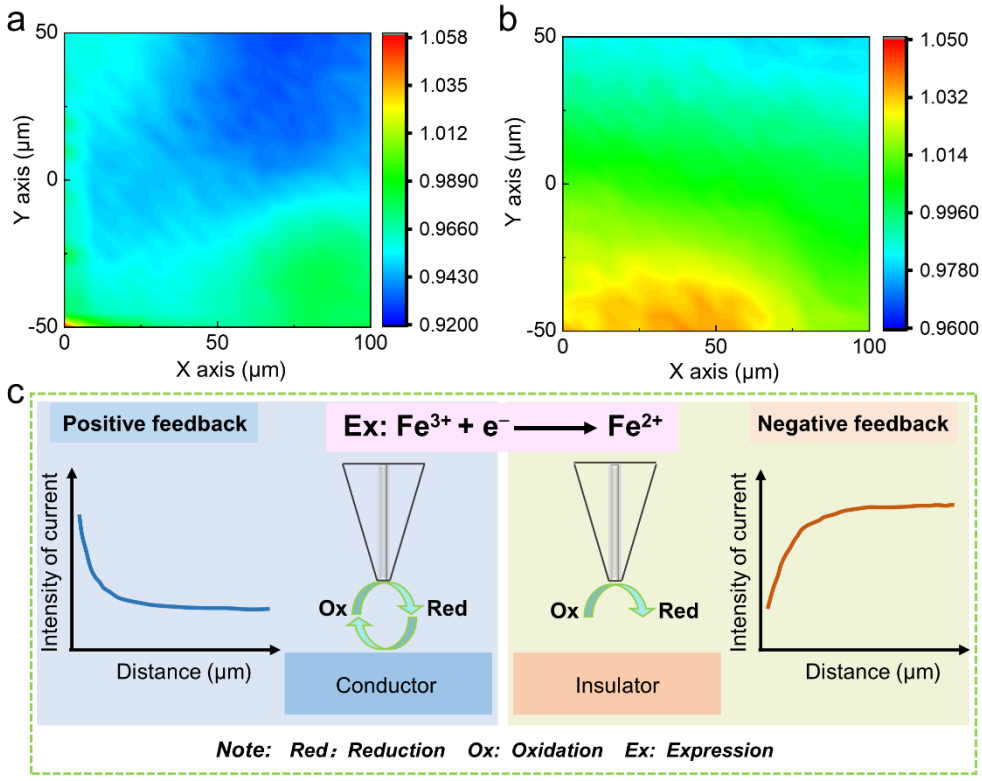

Fig. S14 The corresponding SECM images of the Zn anode after 10 cycles: (a) the baseline electrolyte and (b) the binary electrolyte. (c) Schematic work principle of the SECM technology.

The test principle of SCEM technology:

When the probe (*i.e.*, an ultramicrodisk electrode, UMDE) and the substrate are simultaneously immersed in a solution containing the electroactive substance (labeled as *O*), a potential (E_t) is applied to the probe to make *O* undergo a reduction reaction. When the probe is close to the conductive substrate, its potential is controlled at oxidation potential, and the substrate products can diffuse back to the probe surface to increase the probe current. The closer the probe is to the substrate sample, the greater the current (Fig. S14c). This process is called “positive feedback”. When the substrate has an insulating surface, the current is an opposite trend, which is a “negative feedback” process. Usually, SECM is operated by a current method. When the distance between the probe and the substrate is fixed, the current change on the probe will provide the morphology and corresponding electrochemical information of the substrate.

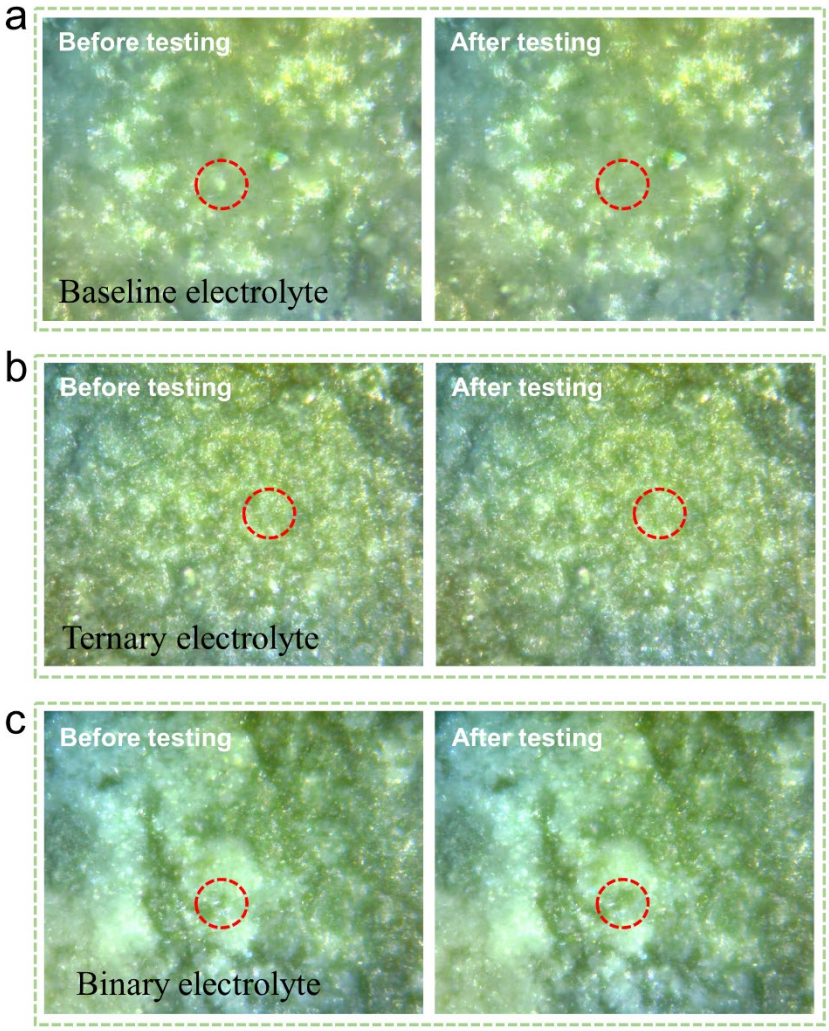

Fig. S15 The optical micrographs of the Zn electrodes before and after the nanoindentation testing: (a) the baseline electrolyte, (b) the ternary electrolyte, and (c) the binary electrolyte.

The Zn surface using the ternary electrolyte has a better ability to maintain structure integrity compared to the baseline electrolyte. For the Zn electrode in the binary electrolyte, the micrographs exhibit a slight change before and after the nanoindentation testing, indicating the less dense Zn^{2+} deposit.

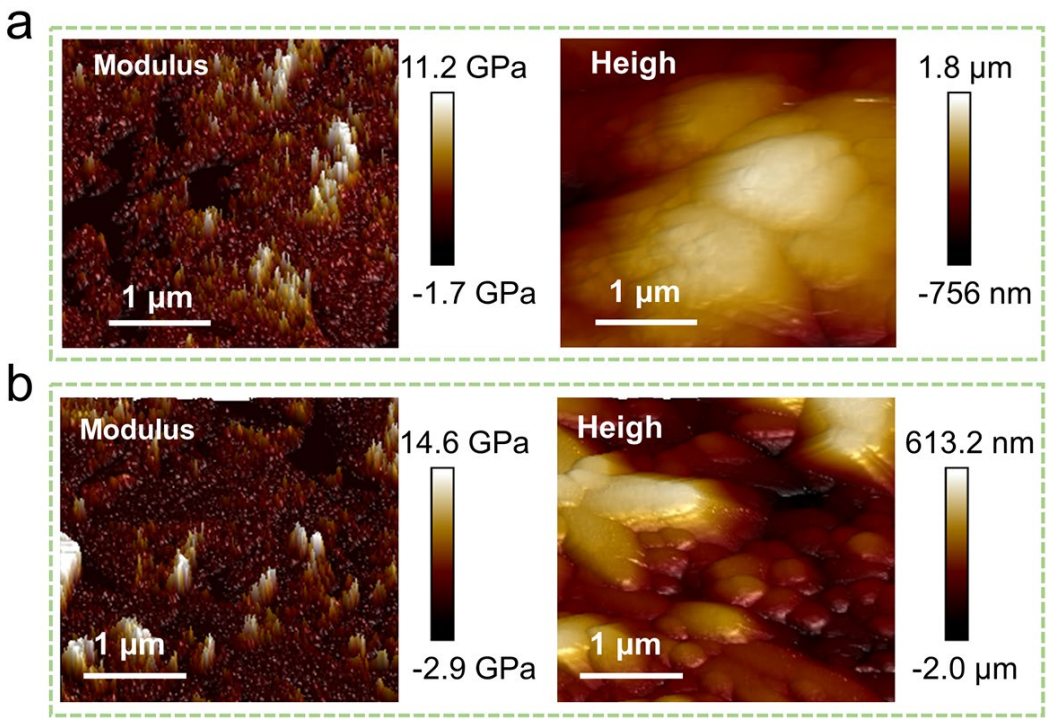

Fig. S16 Mechanical modulus distribution and 3D topographical AFM image of the outside surficial SEI: (a) the baseline electrolyte and (b) the binary electrolyte.

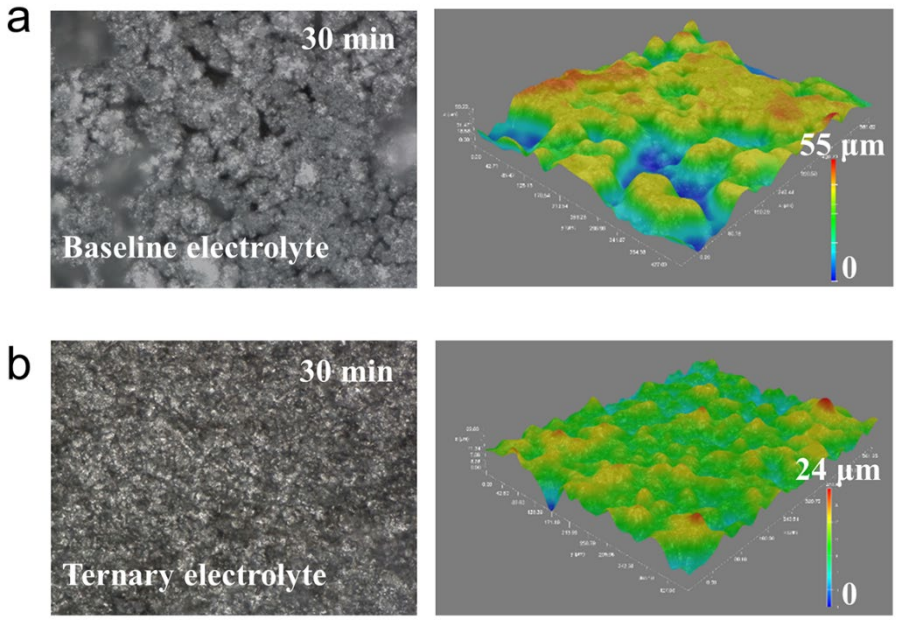

Fig. S17 The LCSM micrographs and the corresponding 3D reconstruction images of the Zn anode after Zn deposition for 30 min in (a) the baseline electrolyte and (b) the ternary electrolyte (Movie S2 and Movie S3).

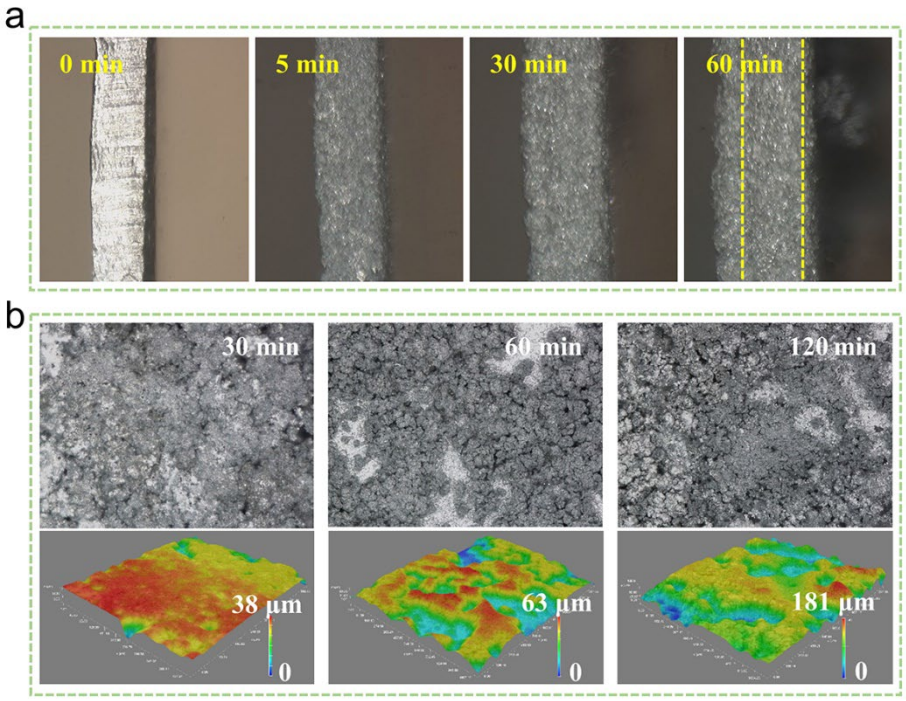

Fig. S18 Zn deposition behavior in the binary electrolyte. (a) *In-situ* optical visualization observations of the Zn deposition process in the binary electrolyte. (b) The LCSM micrographs and the corresponding 3D reconstruction images of the Zn anode after Zn deposition for 30, 60, and 100 min in the binary electrolyte.

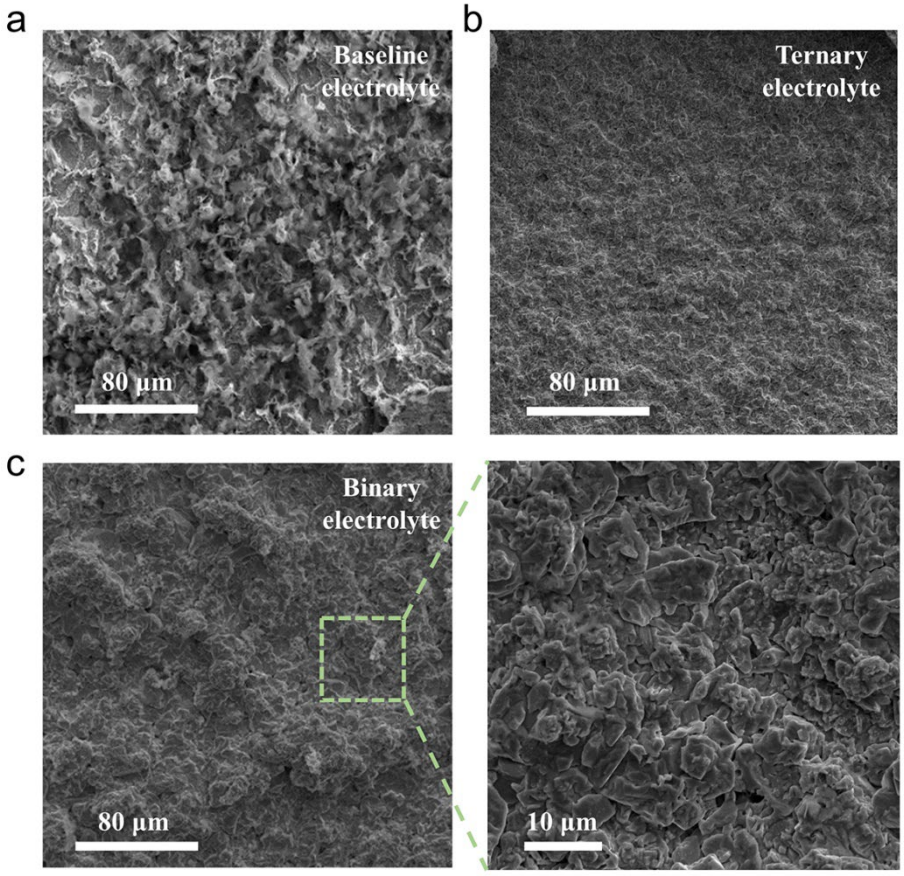

Fig. S19 SEM image of the Zn anodes after Zn deposition for 20 mAh cm^{-2}: (a) the baseline electrolyte and (b) the ternary electrolyte. (c) SEM image of the Zn anodes after Zn deposition for 20 mAh cm^{-2} in the binary electrolyte.

The Zn deposition exhibits mossy and textureless in the baseline electrolyte, while a compact and spherical particle deposition is presented in hybrid electrolytes, especially the ternary electrolyte. This phenomenon is associated with the gradient rigid-soft coupling SEI layer.

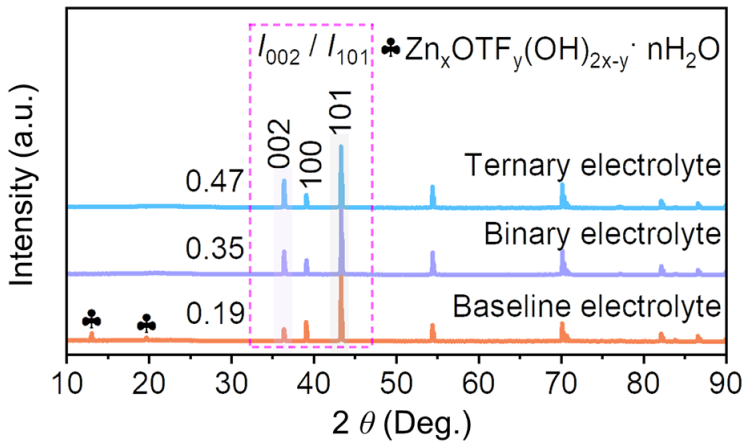

Fig. S20 XRD patterns of Zn anode in various electrolytes after Zn deposition for 20 mAh cm^{-2}.

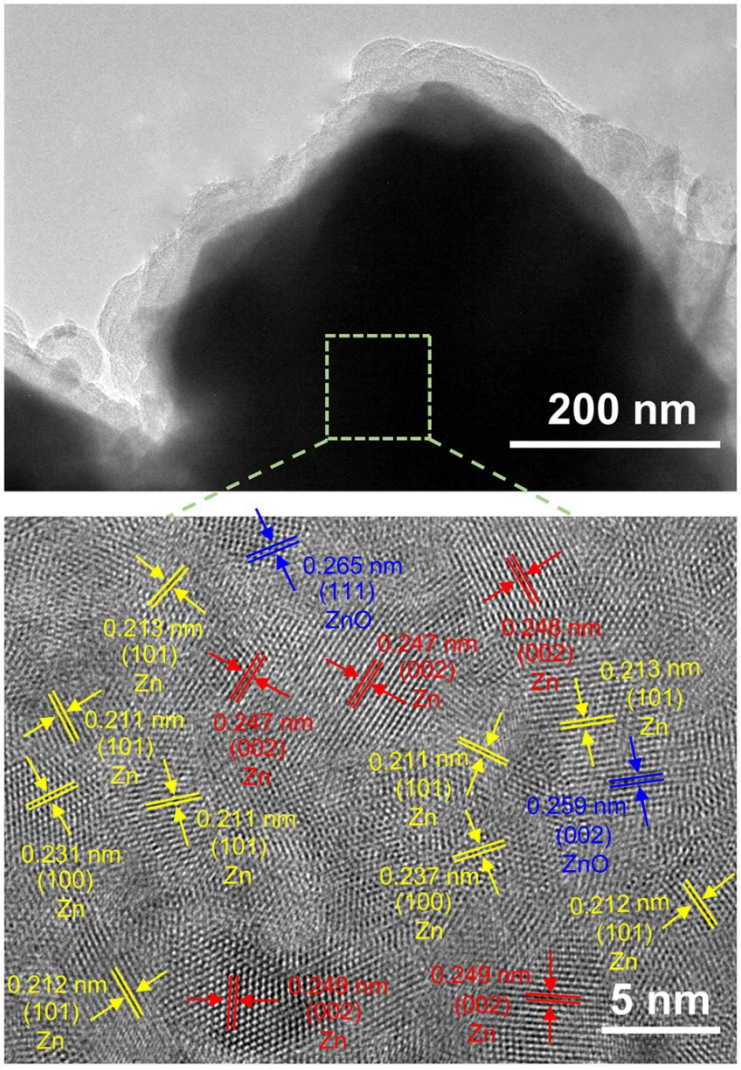

Fig. S21 The TEM image of the deposited Zn in the ternary electrolyte, where the Zn bulk area in the green rectangle is further magnified to analyze the morphology.

Specifically, the Zn metal grows along the (101), (100), and (002) planes. Moreover, the ZnO components with (111) and (002) planes also are found, which may be caused by air oxidation.

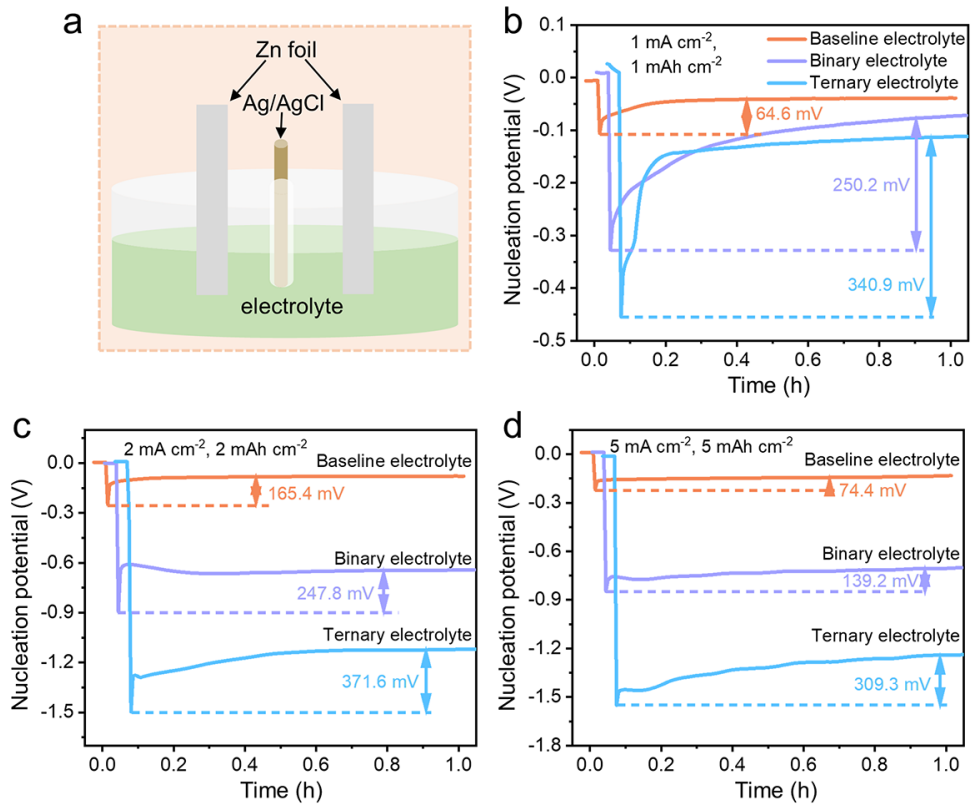

Fig. S22 Nucleation overpotential analysis of the Zn deposition in a three-electrode system using various electrolytes. (a) Schematic illustration of the three-electrode system. Voltage profiles during Zn^{2+} plating at (b) 1 mA cm^{-2}, 1 mAh cm^{-2}, (c) 2 mA cm^{-2}, 2 mAh cm^{-2} and (d) 5 mA cm^{-2}, 5 mAh cm^{-2}.

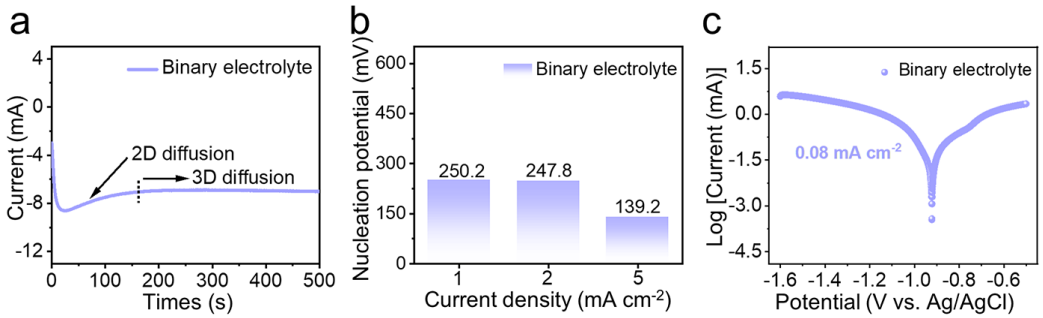

Fig. S23 Zn deposition behavior in the binary electrolyte. (a) Chronoamperometry of Zn metal at a −150 mV overpotential in the binary electrolyte. (b) Nucleation overpotential analysis of the Zn deposition in a three-electrode system using the binary electrolyte. (c) Tafel polarization curve in the binary electrolyte.

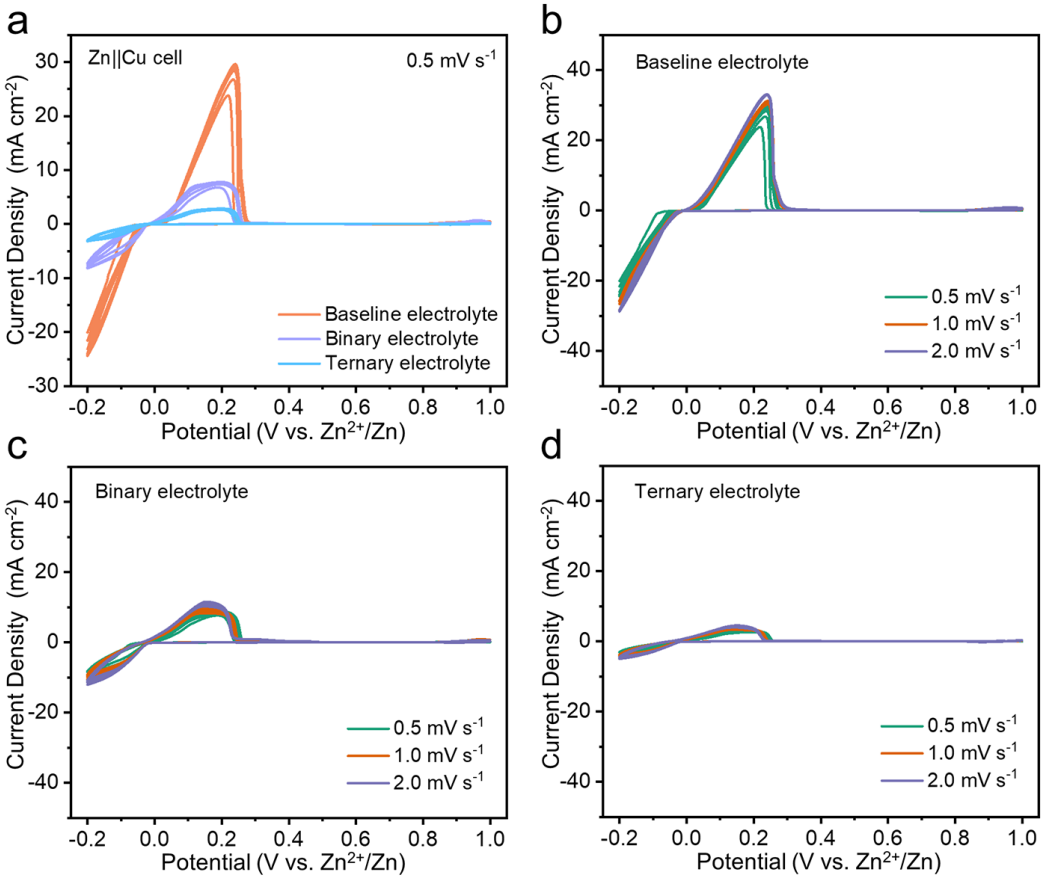

Fig. S24 CV curves of Zn||Cu cells using different electrolytes at different scan rates of 0.5, 1.0, and 2.0 mV s^{-1}. (a) CV curves of Zn||Cu cell in three electrolytes at a scan rate of 0.5 mV s^{-1}. CV curves of Zn||Cu cell in (b) the baseline electrolyte, (c) the binary electrolyte, and (d) the ternary electrolyte.

The CV curves are obtained by the cells after three cycles at every scan rate. The CV curves of Zn||Cu cell in the ternary electrolyte at the same scan rate exhibit better repeatability compared to the baseline electrolyte. The meaningful differences in CV curves verify that the introduction of DMF and DMTFA can suppress side reactions and promote the reversibility of Zn plating/stripping.

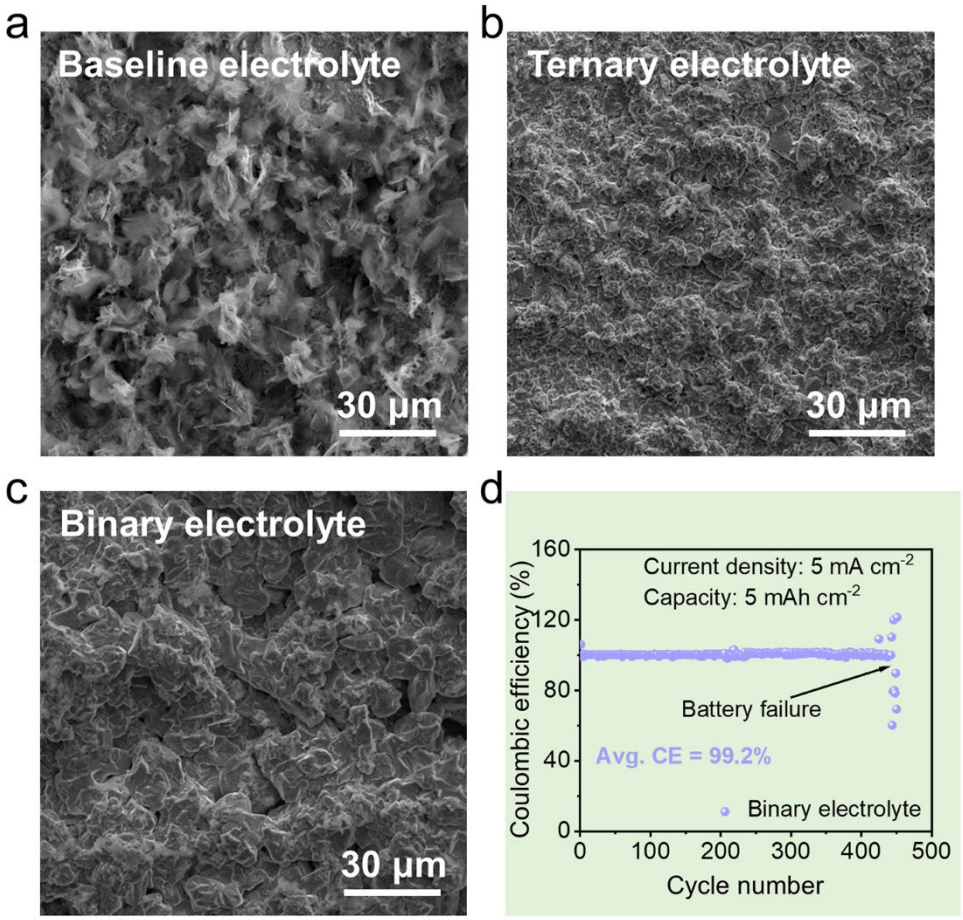

Fig. S25 SEM images of Zn deposition on Cu foils at 5 mA cm^{-2}, 5 mAh cm^{-2} in (a) the baseline electrolyte, (b) the ternary electrolyte, and (c) the binary electrolyte. (d) The Zn plating/stripping CE of the Zn||Cu cells in the binary electrolyte.

The morphology of Zn deposition with mossy and textureless is presented in the baseline electrolyte, while the compact and spherical particle depositions are found in the binary and ternary electrolytes. The compact Zn deposition with small particle size in the ternary electrolyte processes a low surface area, which will be able to suppress interfacial side reactions with the electrolyte, guaranteeing the high reversibility of the Zn electrode. Moreover, the Zn||Cu cell with the binary electrolyte only works for 430 cycles.

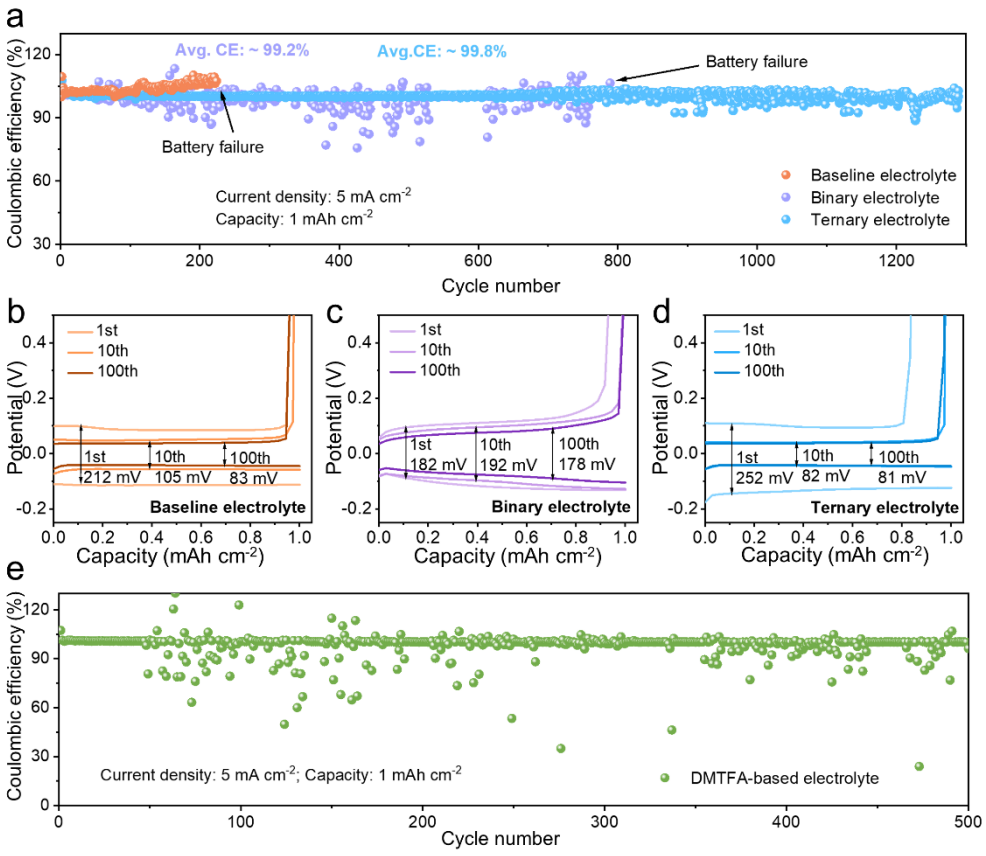

Fig. S26 The cycling performance of Zn plating/stripping in Zn||Cu coin cells at 5 mA cm^{-2} and 1 mAh cm^{-2}. (a) CE tests of Zn||Cu cells under various electrolytes. (b-d) The corresponding voltage curves at the first, 10^{th}, and 100^{th} cycles. (e) CE tests of Zn||Cu cell using the DMTFA-based electrolyte.

The Zn||Cu cell using the ternary electrolyte shows a long cyclic stability over 1290 cycles and always displays small overpotential. It may be because the small spherical particles contribute to making the Zn deposition easier than the mossy Zn deposition. Moreover, the cell exhibits a high average CE of ~ 99.8%. However, the CE of the Zn||Cu cell using the DMTFA-based electrolyte presents obvious fluctuation due to the sedimentation of the undissolved $Zn(OTf)_2$ salt on the electrode surface.

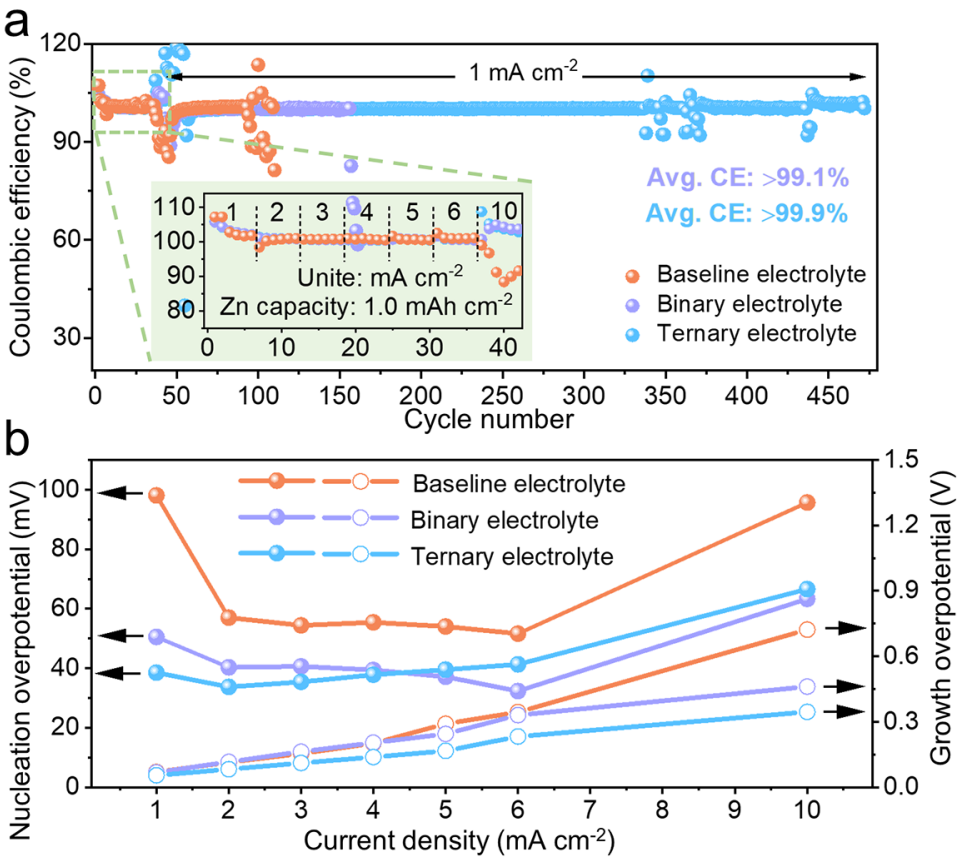

Fig. S27 Rate properties of Zn plating/stripping in Zn||Cu coin cells at various current densities. (a) Rate and cyclic performance of Zn||Cu cells. Insert is further magnified to analyze the rate performance at a Zn capacity of 1.0 mAh cm^{-2}. (b) The nucleation overpotential (solid sphere) and growth overpotential (hollow sphere) of Zn under different electrolytes.

With the increase of current density from 1 to 10 mA cm^{-2}, the CE of Zn||Cu cell with the ternary electrolyte remains relatively stable values. When the current density was switched to 1 mA cm^{-2} for subsequent cycling, the CEs in the hybrid electrolyte still presented insignificant variation, suggesting a benign current adaptivity.

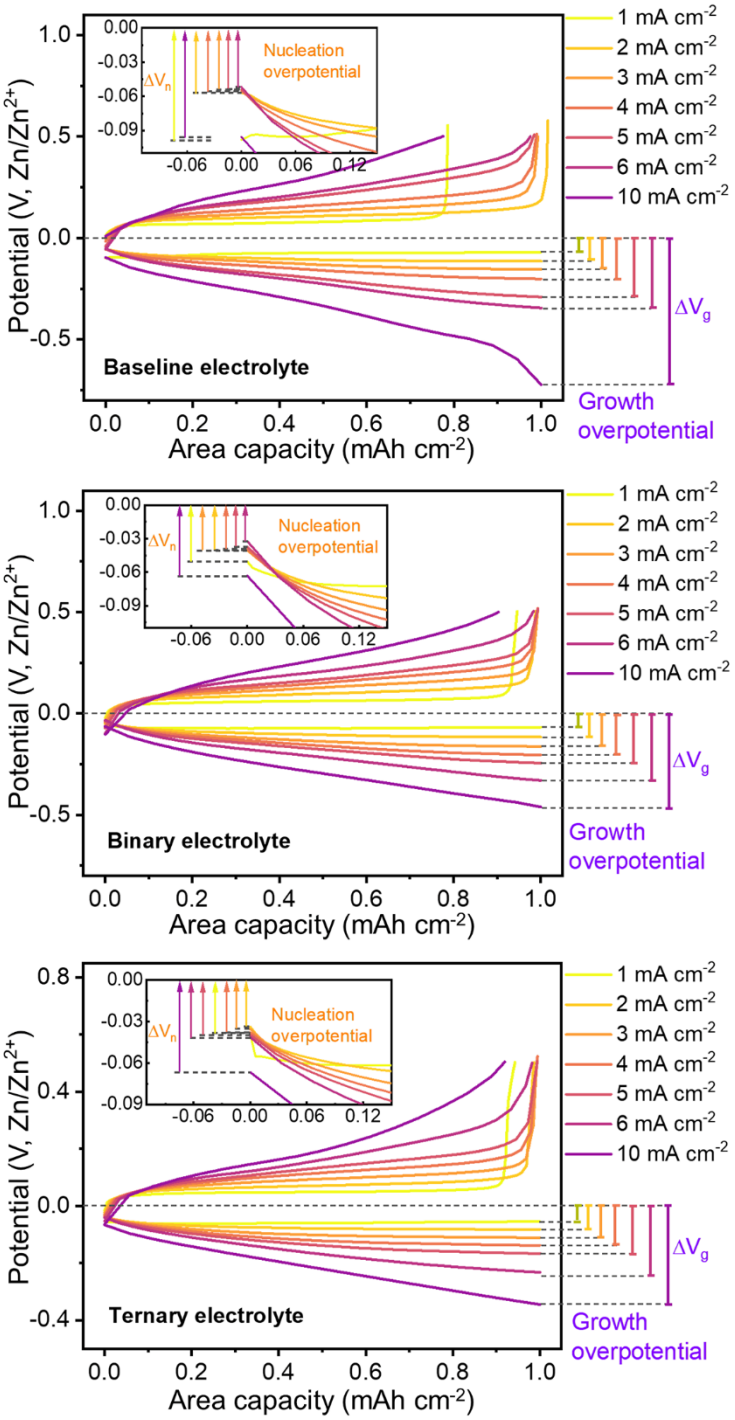

Fig. S28 The voltage curves of Zn||Cu cells at various current densities.

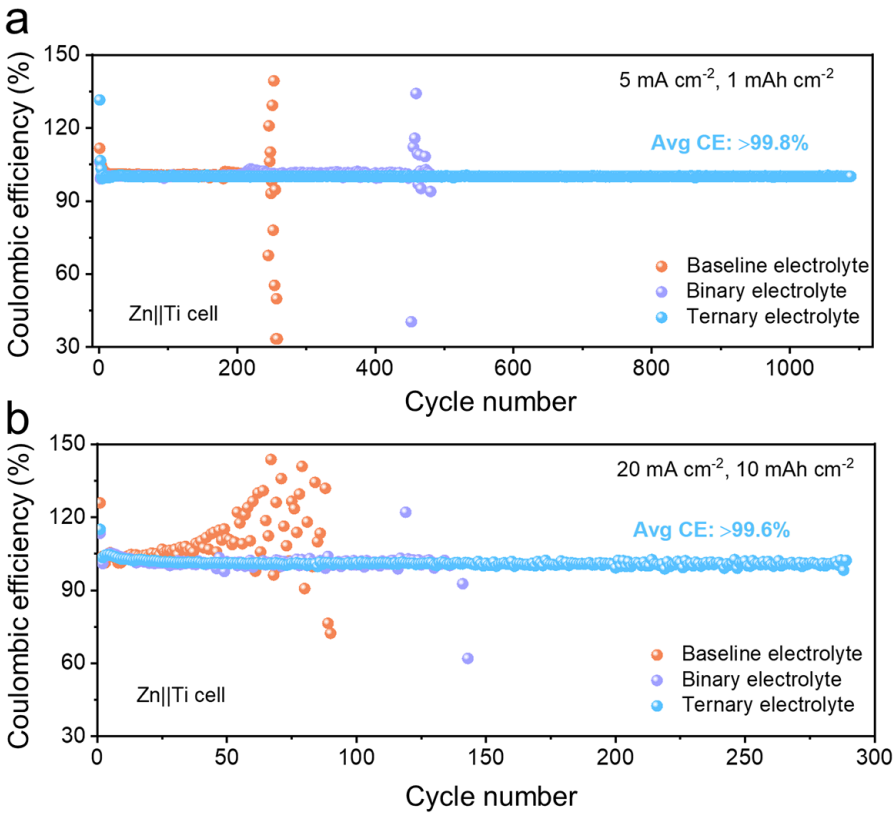

Fig. S29 The reversibility of Zn plating/stripping in Zn||Ti coin cells at 5 and 20 mA cm^{-2}. The long cyclic performances of Zn||Ti cells at various electrolytes: (a) 5 mA cm^{-2}, 1 mAh cm^{-2} and (b) 20 mA cm^{-2}, 10 mAh cm^{-2}.

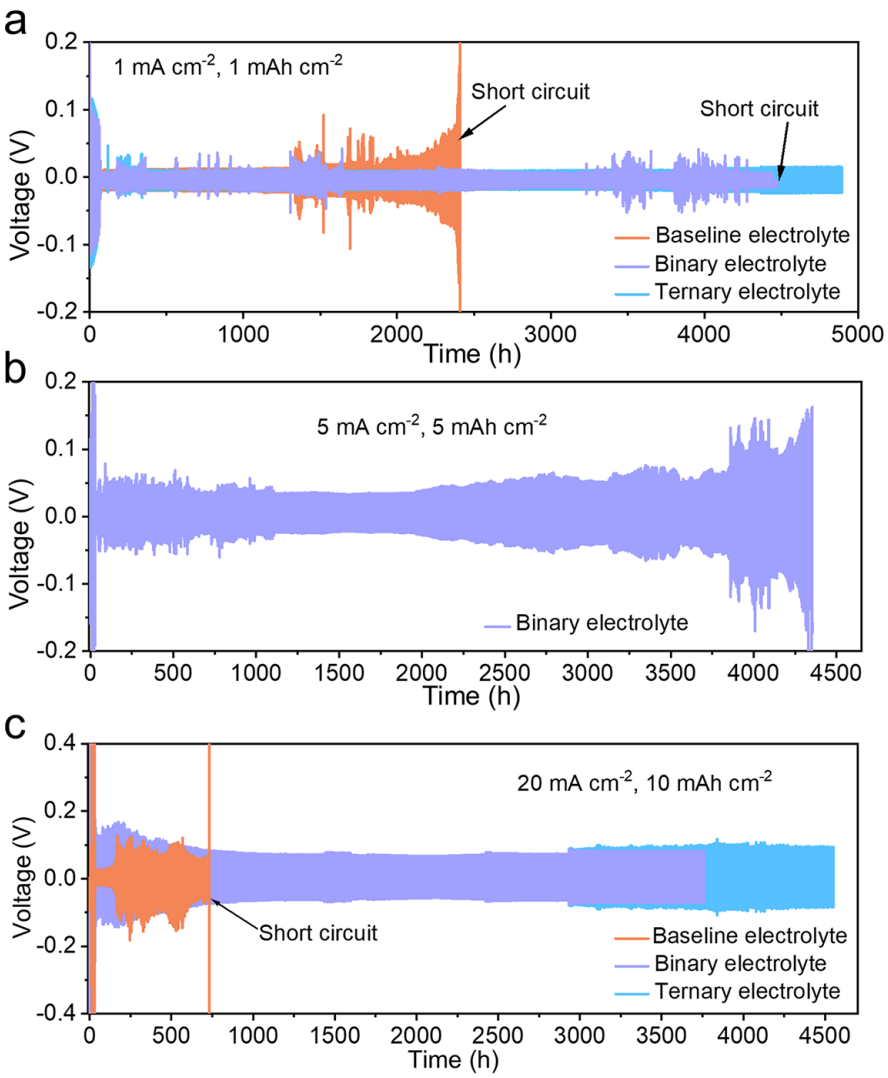

Fig. S30 The reversibility of Zn plating/stripping in Zn||Zn coin cells at different current densities. The long cyclic performances of Zn||Zn cells at various electrolytes: (a) 1 mA cm^{-2} and 1 mAh cm^{-2}, (b) 5 mA cm^{-2} and 5 mAh cm^{-2}, and (c) 20 mA cm^{-2} and 10 mAh cm^{-2}.

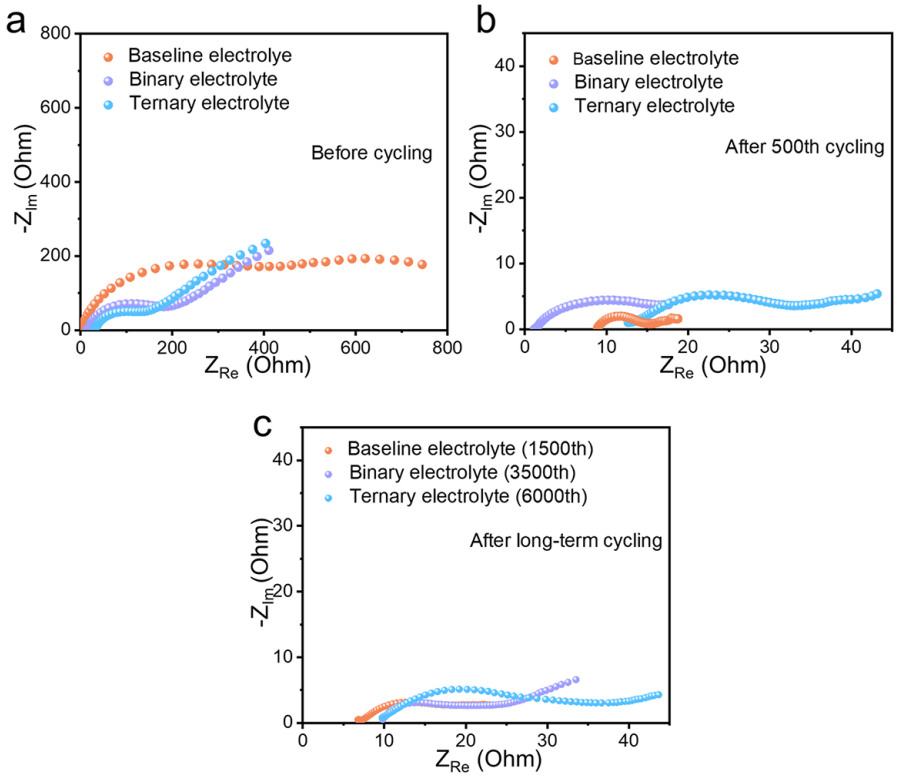

Fig. S31 The EIS results of Zn||Zn coin cells at 5 mA cm^{-2} and 5 mAh cm^{-2}. (a) EIS data of Zn||Zn cells under various electrolytes before cycling. (b) EIS data of Zn||Zn cells under various electrolytes after 500^{th} cycles. (c) EIS date of Zn||Zn cells under various electrolytes after long-term cycling.

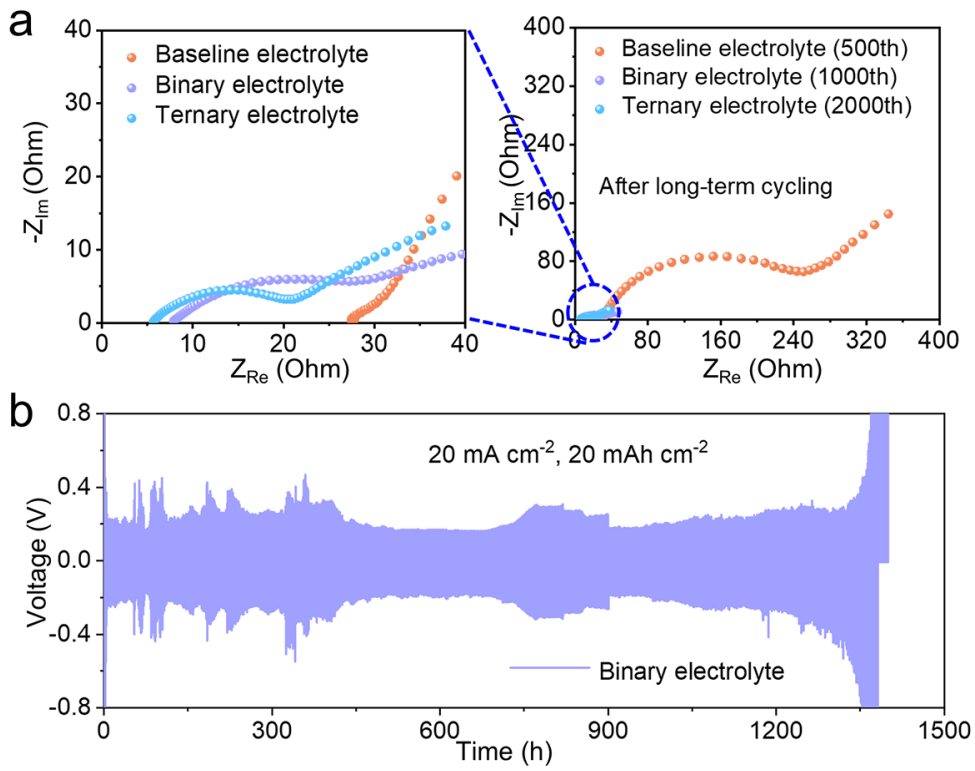

Fig. S32 (a) The EIS results of Zn||Zn coin cells at 20 mA cm^{-2} and 20 mAh cm^{-2} in various electrolytes. (b) The reversibility of Zn plating/stripping in Zn||Zn coin cells with the binary electrolyte at 20 mA cm^{-2} and 20 mAh cm^{-2}.

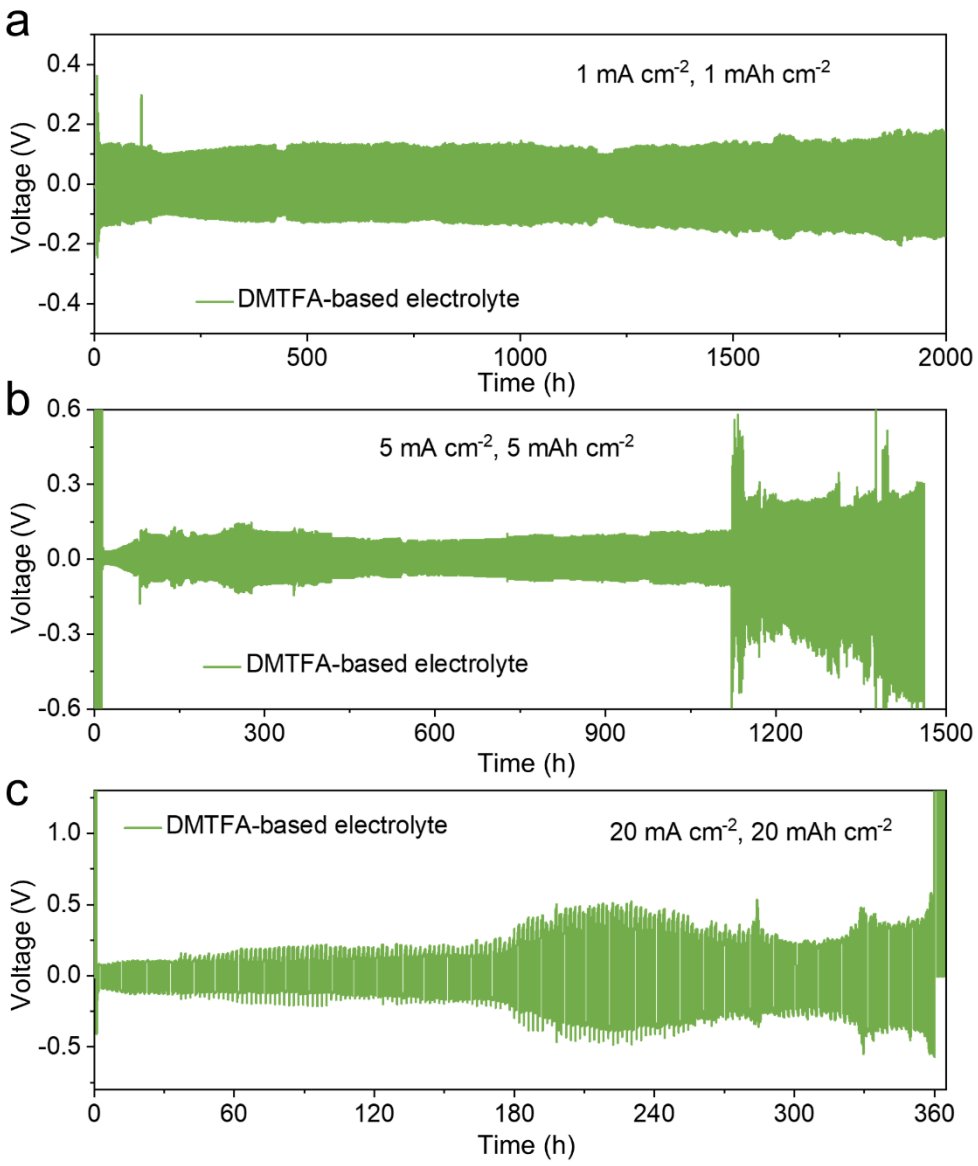

Fig. S33 The reversibility of Zn plating/stripping in Zn||Zn coin cells with the DMTFA-based electrolyte at (a) 1 mA cm^{-2} and 1 mAh cm^{-2}, (b) 5 mA cm^{-2} and 5 mAh cm^{-2}, and (c) 20 mA cm^{-2} and 20 mAh cm^{-2}.

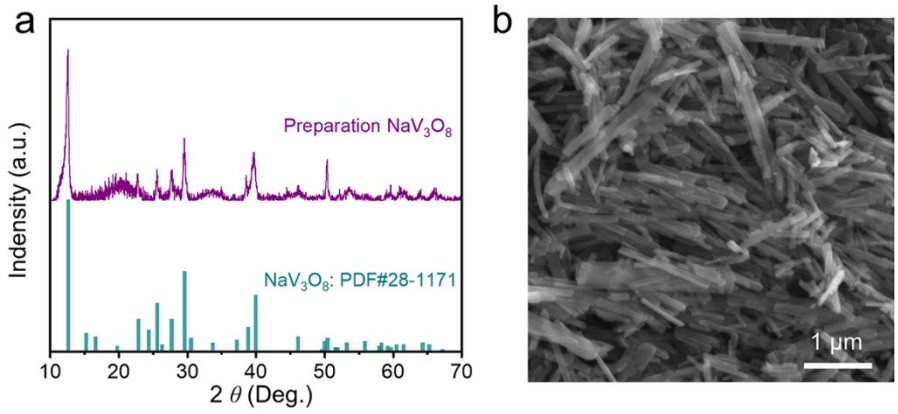

Fig. S33 Characterization of NaV_3O_8 (NVO) cathode material. (a) XRD pattern of the as-synthesized phase NVO. (b) SEM image of the NVO powders.

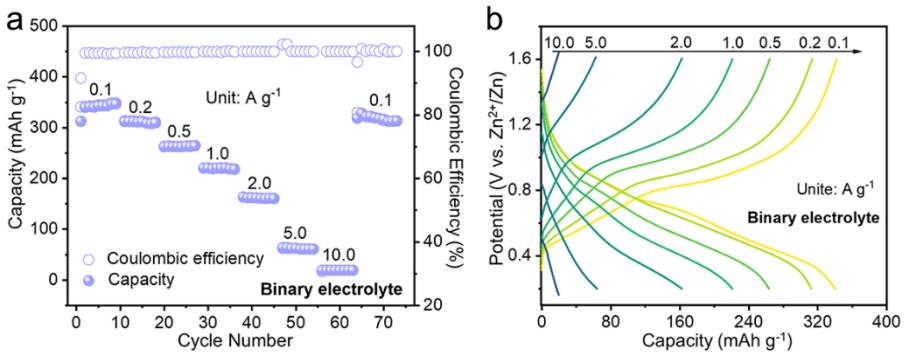

Fig. S34 (a) Rate performance of Zn||NVO coin cells with the binary electrolyte. (b) The corresponding charging/discharging curves at various current densities.

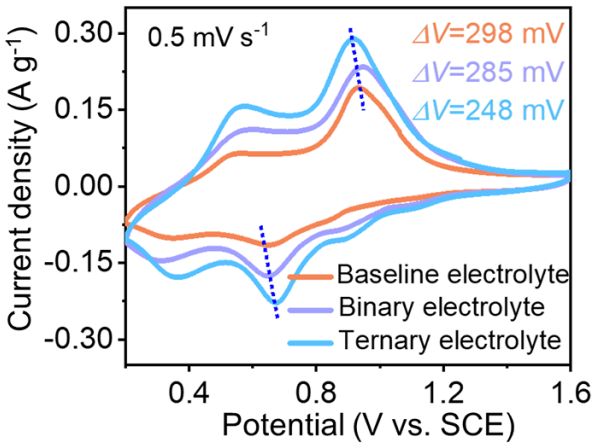

Fig. S35 CV curves of Zn||NVO coin cells with three electrolytes at a scan rate of 0.5 mV s^{-1}.

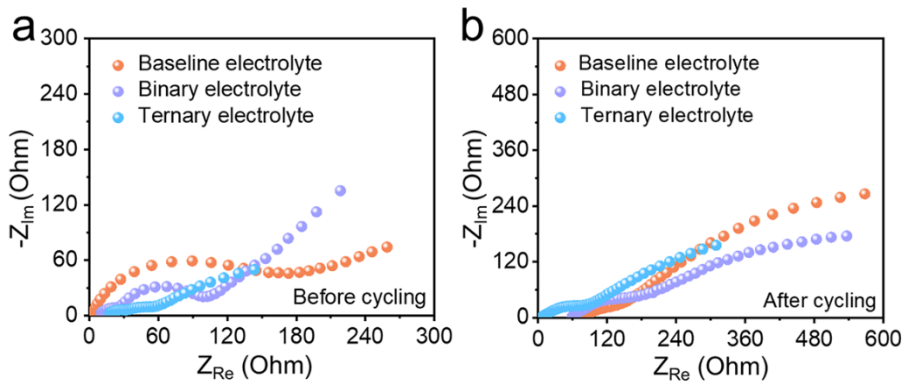

Fig. S36 EIS results of Zn||NVO cell at various electrolytes. (a) EIS data of Zn||NVO cells with various electrolytes before cycling. (b) EIS data of Zn||Zn cells under various electrolytes after rate tests.

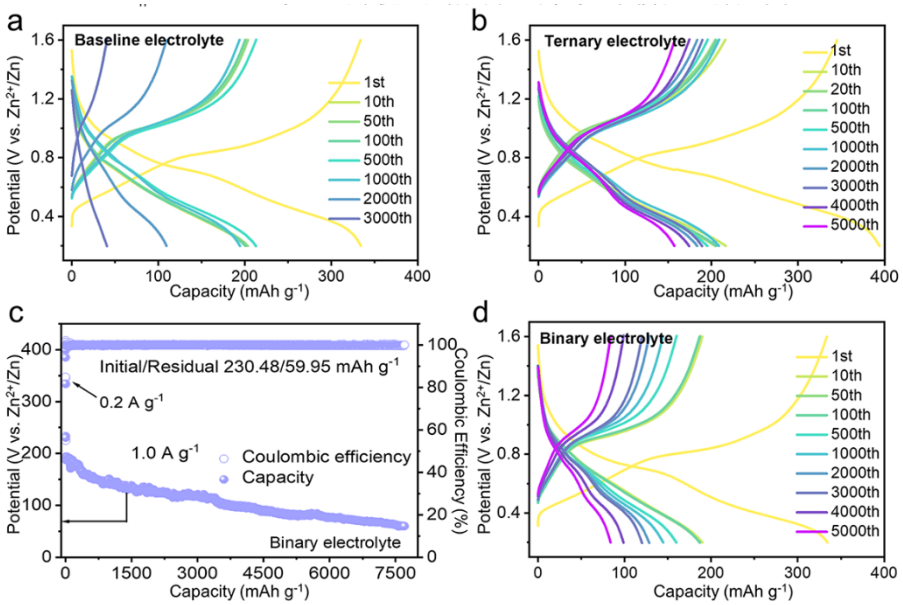

Fig. S37 The galvanostatic charging and discharging profiles of Zn||NVO cell at 1.0 A g^{-1} using (a) the baseline electrolyte and (b) the ternary electrolyte. (c) Cycling performance and (d) the galvanostatic charging and discharging profiles of Zn||NVO coin cell with the binary electrolyte at 1.0 A g^{-1} after three activation cycles at 0.2 A g^{-1}.

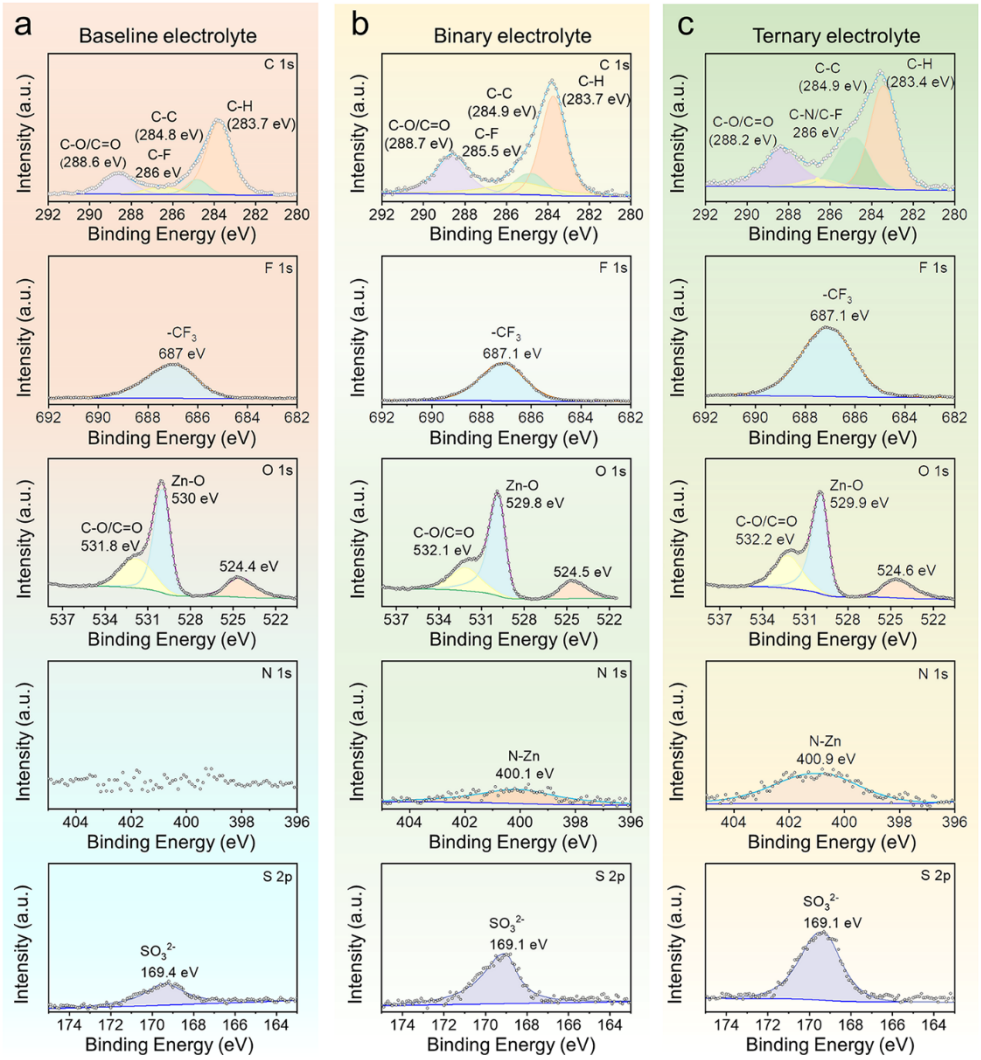

Fig. S38 XPS results of the NVO surface at 0.5 A g^{-1} for 3 cycles under different electrolytes. The C 1s, F 1s, O 1s, N 1s, and S 2p spectra of NVO surface cycles in different electrolytes: (a) the baseline electrolyte, (b) the binary electrolyte, and (c) the ternary electrolyte.

Compared with the CEI at the cathode surface in the baseline electrolyte, the CEI layer formed in the ternary electrolyte exhibits a greatly increased signal of the C-H, C-C, and C-F in C 1s spectra, meanwhile, there are increased signals of the $-CF_3$ and N-Zn as well as $-SO_3^{2-}$ in F 1s, N 1s and S 2p spectra. This again confirms the fact that DMF and DMTFA solvents participate in the Zn^{2+}-solvation structures and promote the construction of the solid-state electrolyte interface, contributing to maintaining the stability of electrodes, which provides high CE and highly stable cycling performances.

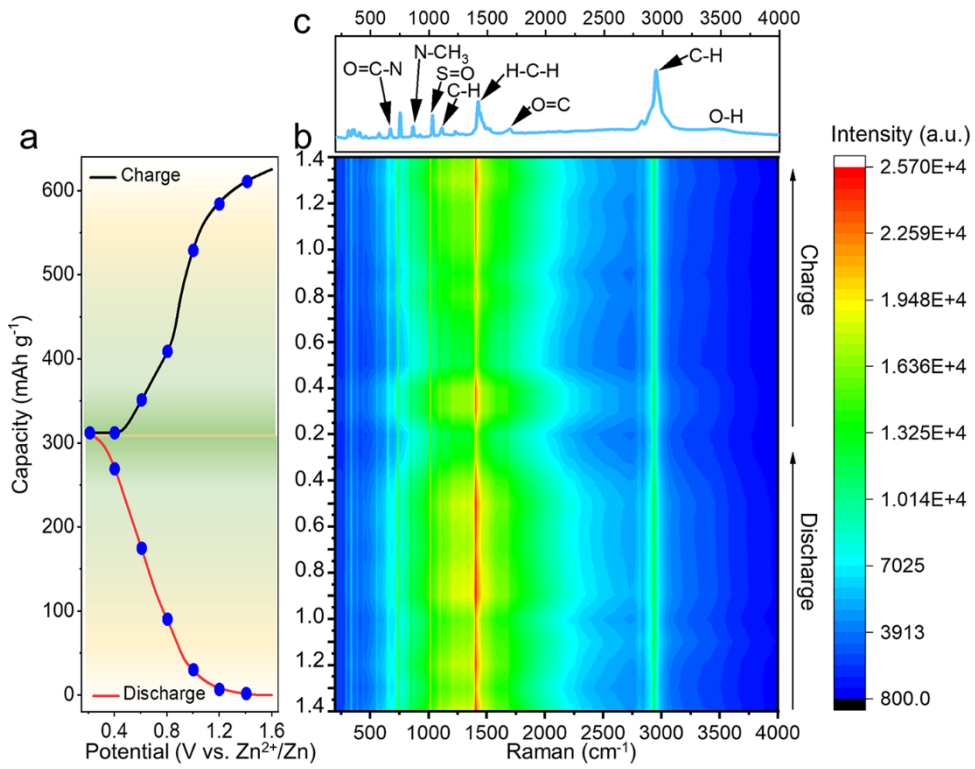

Fig. S39 *In-situ* Raman spectra at different voltages during entire charging and discharging states of Zn||NVO cell with the ternary electrolyte. (a) The entire charging/discharging curves at 0.5 A g^{-1}. (b) Raman spectra of the ternary electrolyte at different voltages. (c) Raman spectra of the ternary electrolyte.

The DMF and DMTFA solvents present typical vibration bands at 665 and 1688 cm^{-1} corresponding to O=C bending and 1112, 1421, and 2944 cm^{-1} corresponding to C-H stretch vibrations. The peak at 1029 cm^{-1} corresponds to the O=S=O wagging vibrations of OTf^- anions. The above-characteristic peak intensities increase during the charging process (0.2~1.6 V) and decrease during the discharging process (1.6~0.2 V), which indicates some physicochemical processes. Significantly, there are rarely additional Raman peaks due to failure to alter the basic vibration mode during the cycling.

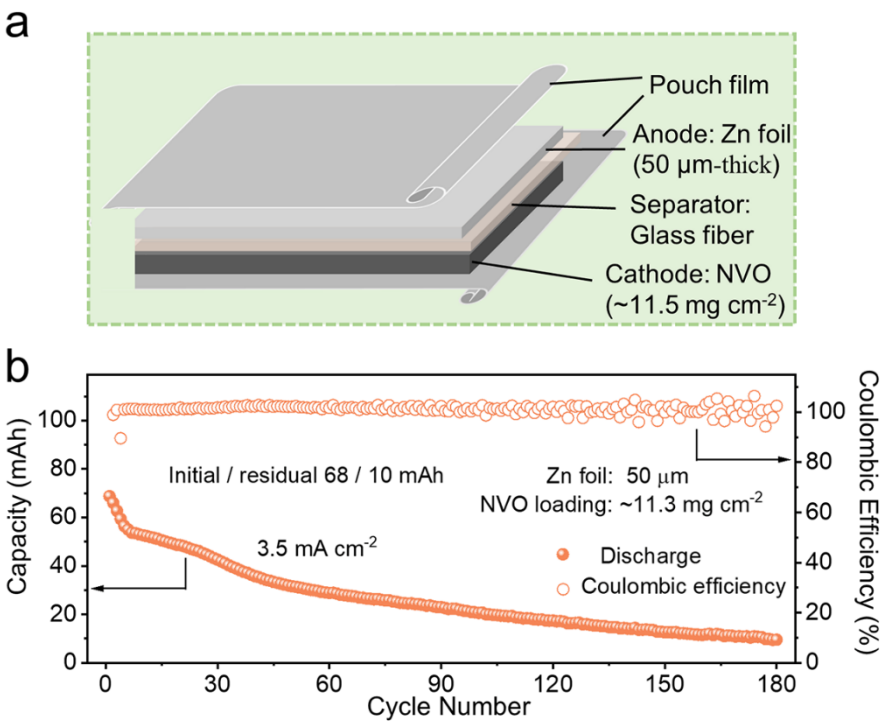

Fig. S40 Pouch cell characterizations of Zn||NVO system. (a) Schematic illustration of Zn||NVO pouch cells. (b) Cycling performance of Zn||NVO pouch cells with the baseline electrolyte at 3.5 mA cm^{-2}.

Table S1 Peak value and intensity ratio of I_{002} and I_{101} in different electrolytes with 10 mA cm^{-2} and 10 mAh cm^{-2}.

	Baseline electrolyte	**Binary electrolyte**	**Ternary electrolyte**
I_{002}	2060	3544	3823
I_{101}	10976	10043	8172
I_{002}/I_{101}	0.1877	0.3529	0.4678

Table S2 Schematic of a three-electrode system and fitting results of the corrosion voltage and corrosion current density of the Zn in various electrolytes.

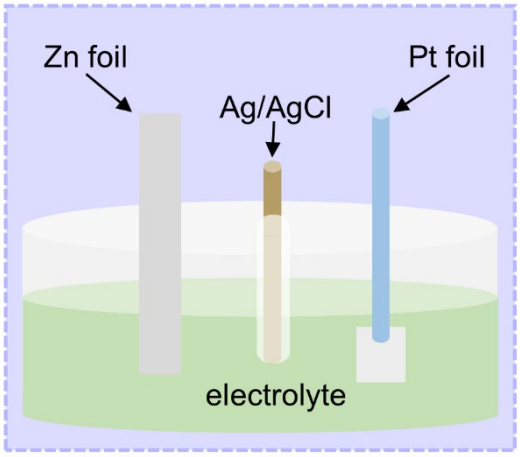

Electrolytes	E_{corr} (V vs. Ag/AgCl)	I_{corr} (mA cm^{-2})	β_a (mV)	β_c (mV)
Baseline electrolyte	−0.935	1.070	100.3	120.8
Binary electrolyte	−0.923	0.080	212.9	166.5
Ternary electrolyte	−0.835	0.010	116.2	120.1

Table S3 Comparison of previously-reported ZIBs used in Fig. 6g of the main text.

Styles	Electrolytes	Current density (mA cm^{-2})	Area capacity (mAh cm^{-2})	Cycling time (h)	Ref.
Additive electrolytes	1 M $ZnSO_4$ + 4 M ChCl	2	2	800	[17]
	4M@CMC | 1M | 4M@CMC ($ZnSO_4$)	10	1	2147	[18]
	2 M $ZnSO_4$ + 50 mM DOTF + H_2O	4	4	350	[19]
	2 M $ZnSO_4$ + 0.5 g L^{-1} Sac	10	10	550	[20]
	2 M $ZnSO_4$ + 0.2 M Gly	4	2	600	[21]
	2 M $Zn(OTf)_2$ + 7 mM DEC	5	5	750	[22]
	2 M $ZnSO_4$ + 0.1 M MSG	20	20	122	[23]
Pure organic electrolytes	0.5 M $Zn(OTf)_2$ + TMP/NMF (*v*: *v*=1: 1)	3	3	750	[24]
	2 M $ZnSO_4$ + DX	10	10	1000	[25]
	4 M $Zn(BF_4)_2$ + EG	0.5	0.25	4000	[26]
	1 M $Zn(BF_4)_2$ + TMP	5	2.5	4200	[27]
Organic/H_2O hybrid electrolytes	2.14 M $Zn(OTf)_2$ + PC/H_2O (*v*: *v*=1: 1)	10	0.5	400	[28]
	2 M $Zn(OTf)_2$ + DME/H_2O (*v*: *v*=4: 6)	10	5	800	[29]
	2 M $ZnCl_2$+SL/H_2O (*v*: *v*=25: 75)	24	24	110	[30]
	0.2 M $Zn(OTf)_2$ + 1.6 M NaOTF + DX/H_2O (*n*: *n*=45.8: 44.2)	0.5	2	4800	[31]

1 M $ZnSO_4$ + DMF/H_2O (*n*: *n*=4: 2)	4	1	1000	[32]
2 M $Zn(CF_3SO_3)_2$+ DMF/H_2O (*n* : *n*=3:7)	0.5	0.5	2000	[33]
0.5 M $ZnSO_4$ + DMF/H_2O (*v*: *v*=7: 3)	3	1	1100	[34]
2 M $ZnSO_4$ + 1-DMA	3	3	1000	[35]
1 M $Zn(OTf)_2$ +0.2 wt% PAN + DMSO/H_2O (*v*: *v*=1:1)	5	1	1250	[36]
3 M $Zn(CH_3SO_3)_2$ + 40 wt% HBCD/60 wt% H_2O	5	5	300	[37]
1 M $Zn(OTF)_2$ + DMAC/TMP/H_2O (*v*: *v*=5: 2: 3)	5	5	1600	[38]
2 M $Zn(OTF)_2$ + AN/H_2O (*v*: *v*=85: 15)	10	1	800	[39]
2 M $Zn(OTf)_2$ + HMPA/H_2O (*v*: *v*=1: 9)	10	10	780	[40]
2 M $Zn(OTf)_2$ + HMPA/H_2O (*v*: *v*=1: 4)	10	10	550	[41]
1.2 M $Zn(OTf)_2$ + DMTFA/DMF/H_2O (*n*: *n*: *n*=1: 1: 1)	5	5	7300	This work
	20	20	4800	
	20	25	2000	

1

2

3

Movie S1 Ignition tests of glass fiber separator saturated with (i) the baseline electrolyte, (ii) the binary electrolyte, and (iii) the ternary electrolyte.

Movie S2 Operando optical video of Zn anode observed in Zn||Zn transparent cell with the baseline electrolyte.

Movie S3 Operando optical video of Zn anode observed in Zn||Zn transparent cell with the ternary electrolyte.

Movie S4 The blue LED screen and fan powered by Zn||Ternary electrolyte||NVO pouch cell.

References

1 M. Frisch, G. Trucks, H. Schlegel, G. Scuseria, M. Robb, J. Cheeseman, G. Scalmani, V. Barone, G. Petersson and H. J. I. Nakatsuji, *Gaussian 16, Revision A. 03, Gaussian*. 3, Wallingford CT, 2016, **3**.

2 P. J. Stephens, F. J. Devlin, C. F. Chabalowski and M. J. Frisch. *J. Phys. Chem*., 1994, **98**, 11623-11627.

3 J. Tirado-Rives and W. L. Jorgensen. *J. Chem. Theory Comput.*, 2008, **4**, 297–306.

4 S. Grimme, J. Antony, S. Ehrlich and H. Krieg, *J. Chem. Phys.*, 2010, **132**, 154104.

5 S. Grimme, S. Ehrlich and L. Goerigk, *J. Comput. Chem.*, 2011, **32**, 1456-1465.

6 T. Lu and F. Chen, *J. Comput. Chem.*, 2012, **33**, 580-592.

7 W. Humphrey, A. Dalke and K. Schulten, *J. Molecular Graphics*, 1996, **14**, 33-38.

8 M. J. Abraham, T. Murtola, R. Schulz, S. Páll, J. C. Smith, B. Hess and E. Lindahl, *SoftwareX*, 2015, **1-2**, 19-25.

9 W. L. Jorgensen, D. S. Maxwell and J Tirado-Rives. *J. Am. Chem. Soc*., 1996, **118**, 11225-11236.

10 O. Acevedo and S. V. Sambasivarao, *J. Chem. Theory Comput.*, 2009, **5**, 1381–1393.

11 W. L. Jorgensen and J. Tirado-Rives, *Proc. Natl. Acad. Sci. USA*, 2005, **102**, 6665-6670.

12 L. S. Dodda, J. Z. Vilseck, J. Tirado-Rives and W. L. Jorgensen, *J. Phys. Chem. B*, 2017, **121**, 3864-3870.

13 L. S. Dodda, I. Cabeza de Vaca, J. Tirado-Rives and W. L. Jorgensen, *Nucleic Acids Res.*, 2017, **45**, W331-W336.

14 L. Martinez, R. Andrade, E. G. Birgin and J. M. Martinez, *J. Comput. Chem.*, 2009, **30**, 2157-2164.

15 T. Darden, D. York and L. Pedersen, *J. Chem. Phy.*, 1993, **98**, 10089-10092.

16 K. Momma and F. Izumi, *J. Appl. Crystallogr.*, 2008, **41**, 653-658.

17 X. Nie, L. Miao, W. Yuan, G. Ma, S. Di, Y. Wang, S. Shen and N. Zhang, *Adv. Funct. Mater.*, 2022, **32**, 2203905.

18 H. Lu, D. Zhang, Q. Jin, Z. Zhang, N. Lyu, Z. Zhu, C. Duan, Y. Qin and Y. Jin, *Adv. Mater.*, 2023, e2300620.
19 C. Li, A. Shyamsunder, A. G. Hoane, D. M. Long, C. Y. Kwok, P. G. Kotula, K. R. Zavadil, A. A. Gewirth and L. F. Nazar, *Joule*, 2022, **6**, 1103-1120.
20 C. Huang, X. Zhao, S. Liu, Y. Hao, Q. Tang, A. Hu, Z. Liu and X. Chen, *Adv. Mater.*, 2021, **33**, e2100445.
21 Q. Gou, H. Luo, Q. Zhang, J. Deng, R. Zhao, O. Odunmbaku, L. Wang, L. Li, Y. Zheng, J. Li, D. Chao and M. Li, *Small*, 2023, e2207502.
22 L. Miao, R. Wang, S. Di, Z. Qian, L. Zhang, W. Xin, M. Liu, Z. Zhu, S. Chu, Y. Du and N. Zhang, *ACS Nano*, 2022, **16**, 9667-9678.
23 Y. Zhong, Z. Cheng, H. Zhang, J. Li, D. Liu, Y. Liao, J. Meng, Y. Shen and Y. Huang, *Nano Energy*, 2022, **98**, 107220.
24 A. Naveed, G. Li, A. Ali, M. Li, T. Wan, M. Hassan, X. Wang, P. Ye, X. Li, Y. Zhou, M. Su, R. Guo, Y. Liu, H. Xu and D. Chu, *Nano Energy*, 2023, **107**, 108175.
25 T. Wei, Y. Ren, Y. Wang, L. Mo, Z. Li, H. Zhang, L. Hu and G. Cao, *ACS Nano*, 2023, **17**, 3765-3775.
26 D. Han, C. Cui, K. Zhang, Z. Wang, J. Gao, Y. Guo, Z. Zhang, S. Wu, L. Yin, Z. Weng, F. Kang and Q.-H. Yang, *Nat. Sustain.*, 2021, **5**, 205-213.
27 G. Ma, S. Di, Y. Wang, W. Yuan, X. Ji, K. Qiu, M. Liu, X. Nie and N. Zhang, *Energy Storage Mater.*, 2023, **54**, 276-283.
28 F. Ming, Y. Zhu, G. Huang, A. H. Emwas, H. Liang, Y. Cui and H. N. Alshareef, *J. Am. Chem. Soc.*, 2022, **144**, 7160-7170.
29 G. Ma, L. Miao, Y. Dong, W. Yuan, X. Nie, S. Di, Y. Wang, L. Wang and N. Zhang, *Energy Storage Mater.*, 2022, **47**, 203-210.
30 M. Wang, J. Ma, Y. Meng, J. Sun, Y. Yuan, M. Chuai, N. Chen, Y. Xu, X. Zheng, Z. Li and W. Chen, *Angew. Chem. Int. Ed. Engl.*, 2023, **62**, e202214966.
31 Y. Yang, G. Qu, H. Wei, Z. Wei, C. Liu, Y. Lin, X. Li, C. Han, C. Zhi and H. Li, *Adv. Energy Mater.*, 2023, **13**, 2203729.
32 P. Xiong, Y. Kang, N. Yao, X. Chen, H. Mao, W.-S. Jang, D. M. Halat, Z.-H. Fu,

M.-H. Jung, H. Y. Jeong, Y.-M. Kim, J. A. Reimer, Q. Zhang and H. S. Park, *ACS Energy Lett.*, 2023, **8**, 1613-1625.

33 Y. Ma, Q. Zhang, L. Liu, Y. Li, H. Li, Z. Yan and J. Chen, *Natl. Sci. Rev.*, 2022, **9**, nwac051.

34 P. Zou, R. Lin, T. P. Pollard, L. Yao, E. Hu, R. Zhang, Y. He, C. Wang, W. C. West, L. Ma, O. Borodin, K. Xu, X. Q. Yang and H. L. Xin, *Nano Lett.*, 2022, **22**, 7535-7544.

35 W. Deng, Z. Xu and X. Wang, *Energy Storage Mater.*, 2022, **52**, 52-60.

36 Z. Liu, J. Ma, X. Liu, H. Wu, D. Wu, B. Chen, P. Huang, Y. Huang, L. Wang, Z. Li and S. Chou, *Chem. Sci.*, 2023, DOI: 10.1039/d2sc06276c.

37 J. Wei, P. Zhang, T. Shen, Y. Liu, T. Dai, Z. Tie and Z. Jin, *ACS Energy Lett.*, 2022, **8**, 762-771.

38 Y. Wang, Z. Wang, W. K. Pang, W. Lie, J. A. Yuwono, G. Liang, S. Liu, A. M. Angelo, J. Deng, Y. Fan, K. Davey, B. Li and Z. Guo, *Nat. Commun.*, 2023, **14**, 2720.

39 C. Meng, W. He, Z. Kong, Z. Liang, H. Zhao, Y. Lei, Y. Wu and X. Hao, *Chem. Eng. J.*, 2022, **450**, 138265.

40 Z. Huang, Z. Li, Y. Wang, J. Cong, X. Wu, X. Song, Y. Ma, H. Xiang and Y. Huang, *ACS Energy Lett.*, 2022, **8**, 372-380.

41 D. Wang, D. Lv, H. Peng, C. Wang, H. Liu, J. Yang and Y. Qian, *Angew. Chem. Int. Ed. Engl.*, 2023, e202310290.